Nano-Micro Letters

e-ISSN 2150-5551
CN 31-2103/TB

REVIEW

https://doi.org/10.1007/s40820-024-01555-6

Cite as
Nano-Micro Lett.
(2025) 17:83

Received: 8 August 2024
Accepted: 30 September 2024

Atomically Precise Cu Nanoclusters: Recent Advances, Challenges, and Perspectives in Synthesis and Catalytic Applications

Mengyao Chen[1], Chengyu Guo[1], Lubing Qin[1], Lei Wang[1], Liang Qiao[2], Kebin Chi[2], Zhenghua Tang[1,3] ✉

HIGHLIGHTS

- Summarizing recent advances on synthesis and catalytic applications of Cu nanoclusters.
- The structure–property–functionality relationship is clearly elucidated.
- Critical analysis of the current challenges and future perspectives.

ABSTRACT Atomically precise metal nanoclusters are an emerging type of nanomaterial which has diverse interfacial metal–ligand coordination motifs that can significantly affect their physicochemical properties and functionalities. Among that, Cu nanoclusters have been gaining continuous increasing research attentions, thanks to the low cost, diversified structures, and superior catalytic performance for various reactions. In this review, we first summarize the recent progress regarding the synthetic methods of atomically precise Cu nanoclusters and the coordination modes between Cu and several typical ligands and then discuss the catalytic applications of these Cu nanoclusters with some explicit examples to explain the atomical-level structure–performance relationship. Finally, the current challenges and future research perspectives with some critical thoughts are elaborated. We hope this review can not only provide a whole picture of the current advances regarding the synthesis and catalytic applications of atomically precise Cu nanoclusters, but also points out some future research visions in this rapidly booming field.

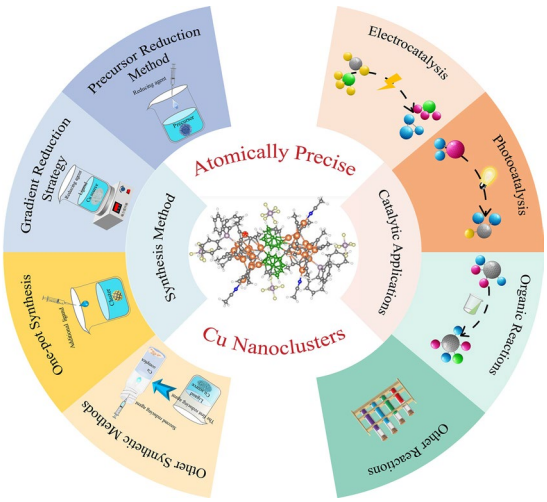

KEYWORDS Atomically precise Cu nanoclusters; Controllable synthesis; Catalytic applications; Structure–performance relationship; Challenges and perspectives

✉ Zhenghua Tang, zhht@scut.edu.cn
[1] New Energy Research Institute, School of Environment and Energy, South China University of Technology, Guangzhou Higher Education Mega Centre, Guangzhou 510006, People's Republic of China
[2] Petrochemical Research Institute, PetroChina Company Limited, Beijing 102206, People's Republic of China
[3] Key Laboratory of Functional Inorganic Material Chemistry (Heilongjiang University), Ministry of Education, Harbin 150001, People's Republic of China

Published online: 03 December 2024

1 Introduction

1.1 Uniqueness of Atomically Precise Cu Nanoclusters

The last decade has witnessed the great success of nanoscience and nanotechnology, yet ideal research model with well-defined composition and structure is still lacking. Specifically, most of the studied nanomaterials are quite polydisperse, that means, in most studied systems, the nano-scientists are extremely difficult to find two same nanoparticles with identical size, morphology, composition, and structure. To advance nanoscience and nanotechnology, one of the ultimate goals for the nano-scientists is to find a truly uniform system, in another word, atomically precise nanoparticles as research models [1, 2].

The emergence of atomically precise coinage metal (Au, Ag, Cu, and its alloy, etc.) nanoclusters can realize such goal [1]. Atomically precise metal nanocluster is a novel type of nanomaterial with the size in the sub-nanometer regime, normally 1–3 nm in diameter. It usually comprises 10–300 metal atoms with surface ligand as the protecting agents capping on the metal core. Note that as the nanoparticle size decreases downward to the sub-nanometer range, due to the strong quantum confinement effect, distinctly different physicochemical properties of metal nanoclusters from relatively large metal nanoparticles are observed [3]. For instance, discrete optical absorbance features can be readily identified in molecular Au nanoclusters, but such feature is absent in larger Au nanoparticle counterparts [4]. More importantly, the sub-nanometer size of the metal nanocluster is still within the resolving limitation of single crystal X-ray diffraction (SC-XRD), that allows nano-chemists to resolve their structure with atomic precision [5]. Such precise structure cannot be available for many other nanomaterials, which render metal nanoclusters unique advantages to comprehensively study the structure–property relationship in various fields, such as sensing [6, 7], assembly [8, 9], catalysis [10–12], optoelectronic [13, 14], and cancer therapy [15–17]. Furthermore, the chemical stability of these metal nanoclusters in terms of electronic structure can be explained by the "superatom" theory, where the electrons are confined in the spherical metal core of a jellium model [18]. It is believed that if the free electron number of a cluster is in good agreement of inert gas atoms (e.g., 2, 8, 18, 34, 52 electrons in the outmost orbital for He, Ne, Ar, Kr, Xe), it can be considered as a superatom having robust stability [18]. Meanwhile, the thermodynamic stability of thiolate metal nanoclusters is associated with the energy balance between the adsorption strength of the ligand shell to the metal core and the cohesive energy of the metal core [19]. In addition, for the non-magic number metal nanoclusters, the Wang group developed a superatomic orbital splitting (SOS) theory to understand the electronic configuration, where the shape of the metal core is considered in determining the order of the group orbital levels [20].

It is worth noting that, compared with noble metal nanoclusters such as Au, Ag, Pd, and Pt, Cu nanoclusters possess some unique characteristics. First, Cu is more earth abundant hence can be more cost effective for large-scale production to prepare functional nanomaterials. Secondly, Cu possesses different valence states including $0, +1, +2$, which render Cu atom with different spatial arrangement in the metal core. So far, superatomic Cu nanoclusters with Cu(0) core, Cu(I) clusters, and Cu(II) complexes have been extensively reported [21, 22]. It is worth noting that different charge states impart Cu nanomaterial with drastically different physicochemical properties and reactivities, and the variation of the valence state during some catalytic reaction has also been observed [23–25]. Finally, Cu nanoclusters hold some peculiar functionalities that are not available from other noble metal nanoclusters [26]. For instance, Cu has good adsorption for CO_2 than hydrogen, and it has strong capability to construct C–C bond, so in electrochemical CO_2 reduction, using Cu nanoclusters can suppress the hydrogen evolution reaction and obtain HCO_2H, CH_3OH, CH, and even more valuable C2+ products such as C_2H_4 and C_2H_5OH [27], while only CO can be acquired when using Au or Ag nanoclusters as catalysts in most cases [28–34]. Table 1 summarizes all the Cu nanoclusters which have been discussed in this paper.

1.2 Cu–Ligand Coordination Modes in Cu Nanoclusters

To prevent the Cu atoms from agglomeration or aggregation, surface capping ligand is critical as the stabilizing agent to allow Cu atoms to form a certain small core but not into a bulky core or an agglomerate. Furthermore, the ligand can significantly affect the physical and chemical properties of Cu nanoclusters through binding with the surface Cu atoms [67–69]. These interfacial coordination moieties form the ligament between the metal core and the surface ligands, and such ligament governs

https://doi.org/10.1007/s40820-024-01555-6

Table 1 The formula, metal core configuration, and catalytic reaction of Cu nanoclusters discussed in this paper

Formulas	Cluster configuration	Catalytic reaction	Refs.
$[Cu_6(MBD)_6]$	Octahedron	CO_2RR	[27]
$[Cu_{29}Cl_4H_{22}(Ph_2phen)_{12}]Cl$	$Cu_{13}@Cu_{16}$	–	[35]
$[Cu_{20}(C{\equiv}CPh)_{12}(OAc)_6)]$	$Cu_4@Cu_{16}$	[3 + 2] Cycloaddition	[36]
$[Cu_{53}(C{\equiv}CPhPh)_9(dppp)_6Cl_3(NO_3)_9]$	Layer-structure	–	[37]
$[Cu_{26}(DPPE)_3(CF_3CO_2)_8(CH_3O)_2(^tBuC{\equiv}C)_4H_{11}]^+$	$Cu_4@Cu_6@Cu_{16}$	CO_2RR	[38]
$[Cu_{32}(PET)_{24}H_8Cl_2](PPh_4)_2$	$Cu_{18}@Cu_4PET_2@$ $Cu_{14}(PET)_{22}Cl_2$	Carbonylation of aniline	[39]
$[Cu_{25}H_{22}(PPh_3)_{12}]Cl$	$Cu_{13}@Cu_{12}$	–	[40]
$[Cu_{18}H_{17}(PPh_3)_{10}]Cl$	$Cu_8@Cu_{10}$	–	[41]
$[Cu_{18}H_3(S\text{-}Adm)_{12}(PPh_3)_4Cl_2]$	$Cu_{10}@Cu_8S_{12}P_4$	–	[42]
$[Cu_{31}(4\text{-}MeO\text{-}PhC{\equiv}C)_{21}(dppe)_3](ClO_4)_2$	$Cu_{13}@Cu_{18}$	–	[43]
$[Cu_6(4\text{-}MeO\text{-}PhC{\equiv}C)_5(dppe)_3](ClO_4)$	Trigonal-prismatic configuration	–	[44]
$[Cu_{50}(CF_3COO)_{12}(3, 5\text{-}di\text{Me-}PhS)_{18}(PPh_3)_4H_2]$	$Cu_{44}@Cu_6$	–	[45]
$[Cu_{41}Cl_2(2\text{-}F\text{-}C_6H_4S)_{12}(CF_3COO)_6(PPh_3)_6H_{19}]^{2-}$	$Cu_{29}@Cu_{12}$	*p*-Nitrophenol reduction	[46]
$[Cu_{41}(2, 5\text{-di-Methyl-}C_6H_3S)_{12}(BO_3)_3Cl_3(PPh_3)_6H_{19}]$	$Cu_{29}@Cu_{12}$	*p*-Nitrophenol reduction	[46]
$[Cu_{23}(^tBuC{\equiv}C)_{13}(CF_3COO)_6]$	$Cu_4@Cu_{19}$	–	[47]
$[Cu_{23}(^tBuC{\equiv}C)_{13}(CF_3COO)_6]{\cdot}CHCl_3$	$Cu_4@Cu_{19}$	–	[47]
$[Cu_{53}(RCOO)_{10}(C{\equiv}C^tBu)_{20}Cl_2H_{18}]^+$	$Cu_3@Cu_{10}Cl_2@Cu_{20}@Cu_{20}$	–	[48]
$[Cu_{13}Na_2(CZ\text{-}PrA)_6(TC4A)_2Cl(CH_3OH)_2]$	$Cu_9@Cu_4$	Sulfide oxidation	[49]
$[Cu_{13}Na(CZ\text{-}PrA)_6(TC4A)_2(CH_3OH)]{\cdot}CH_3OH{\cdot}CH_2Cl_2{\cdot}CH_3COCH_3$	$Cu_9@Cu_4Cl$	Sulfide oxidation	[49]
$[Cu_{13}(S_2CN^nBu_2)_6(C{\equiv}CR)_4](PF_6)$	$Cu@Cu_{12}$ cuboctahedron	–	[50]
$[Cu_{32}H_{20}(S_2P(O^iPr)_2)_{12}]$	$Cu_{14}@Cu_9@Cu_9$	CO_2RR	[51]
$[Cu_8(H)(L1)_6PF_6]$ (L1 = 9H-carbazole-9-carbodithioate)	Cu_4 double tetrahedron	CO_2RR	[52]
$[Cu_8(^tBuS)_4(L1)_4]$ (L1 = 9H-carbazole-9-carbodithioate	Cu_4 double tetrahedron	CO_2RR	[52]
$[Cu_8(^tBuS)_4(L2)_4]$ (L2 = *O*-ethyl carbonodithiolate)	Cu_4 double tetrahedron	CO_2RR	[52]
$[Cu_{13}(C_4B_{10}H_{11})_{10}(PPh_3)_2(CH_3CN)_2](PF_6)_3$	–	Nitrate reduction	[53]
$[Cu_{26}(C_4B_{10}H_{11})_{16}(C_2B_9H_{10}C_2)_2(PPh_3)_2(CH_3CN)_4](PF_6)_4$	–	Nitrate reduction	[53]
$[Cu_6(HL_1)_2(L1)_4(PF_6)_2]$	Cu_6 octahedron	CO_2RR	[54]
$[Cu_{61}(S^tBu)_{26}S_6Cl_6H_{14}]$	$Cu_{19}@Cu_{42}(S^tBu)_{26}S_6Cl_6$	–	[55]
$[Cu_{57}H_{20}(PET)_{36}(TPP)_4]^+$	$Cu_{14}@Cu_{43}S_{36}$	–	[56]
$[Cu_{58}H_{20}PET_{36}(PPh_3)_4]^{2+}$	$Cu_8@Cu_6@Cu_{24}@Cu_{12}@Cu_8$	[3 + 2] Cycloaddition	[57]
$[Cu_{57}H_{20}PET_{36}(PPh_3)_4]^+$	$Cu_8@Cu_6@Cu_{24}@Cu_{12}@Cu_7$	[3 + 2] Cycloaddition	[57]
$[Cu_{28}H_{10}(C_7H_7S)_{18}(TPP)_3]$	$Cu_{13}@Cu_{15}S_{18}P_3$	C−C coupling reaction	[58]
$[Cu_7(SC_5H_9)_7(PPh_3)_3]$	–	C−C coupling reaction	[59]
$[Cu_3(NHC)_3(PF_6)_3]$	–	A^3 coupling and Redox-A^3 coupling reaction	[60]
$[Cu_8(Tf\text{-}dpf)_4(NO_3)_2](NO_3)_2$	Two thin slices of supramolecular layers	"Aldehyde–acetylene–amine" A^3 coupling reaction	[61]
$[Cu_8(L2)_2(L3)_2]$(L2, L3 = deprotonated pyrazole)	–	Synthesis of indolizine	[62]
$Cu_{18}H(PET)_{14}(PPh_3)_6$(isothiocyanate)$_3$	$Cu_{15}@Cu_3$	Reduction of ferricyanide to ferrocyanide	[63]
$[Cu_{66}Cl_8(PPh_3)_8(SC_2H_5)_{32}H_{24}](SbF_6)_2$	Layered arrangement	Hydrogenation of cyclohexanone	[64]
$[Cu_{20}H_9(Tf\text{-}dpf)_{10}]{\cdot}BF_4$	$Cu_{12}@2Cu_4$	Conjugate reduction of cinnamaldehyde	[65]
$[Cu_{20}H_8(Tf\text{-}dpf)_{10}]{\cdot}(BF_4)_2$	$Cu_{12}@2Cu_4$	Conjugate reduction of cinnamaldehyde	[65]
$Se@Cu_{20}(PhSe)_{12}(PPh_3)_2(C_6H_5COO)_6$	$Se@Cu_6@Cu_3@Cu_3@Cu_3@Cu_3@Cu_2$	4-Nitrophenol reduction	[66]
$Se@Cu_{20}(PhSe)_{12}(PPh_3)_2(CF_3COO)_6$	$Se@Cu_6@Cu_3@Cu_3@Cu_3@Cu_3@Cu_2$	4-Nitrophenol reduction	[66]

– denotes none or not available

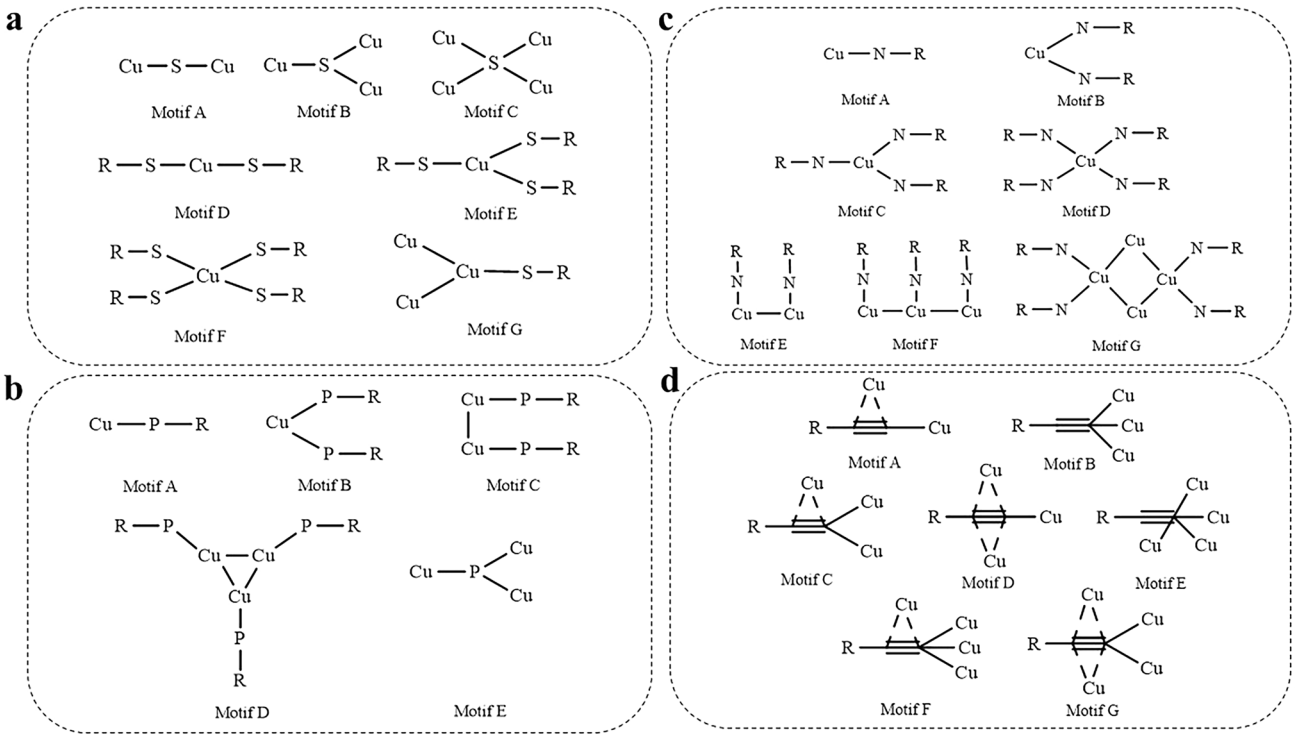

Scheme 1 Metal–ligand coordination modes in Cu nanoclusters. **a** Cu–S coordination modes, **b** Cu–P coordination mode, **c** Cu–N coordination mode, **d** Cu–alkynyl carbon coordination mode

the electron coupling behaviors. So far, various types of molecules have been employed as capping ligand to stabilize the Cu core, and four typical widely employed organic molecules are thiolate [1, 3], phosphine containing molecule [70], nitrogen containing molecule [71], and alkynyl ligand [72, 73], yet they have markedly different coordination modes to bind the Cu atoms (Scheme 1). As illustrated in Scheme 1a, one S atom can coordinate with one, two, three, and four Cu atoms [39], and one Cu atom can coordinate with one, two, three, and four S atoms [74, 75]. One Cu atom can coordinate with one or two P atoms [40, 41], and one P atom can coordinate with three Cu atoms (Scheme 1b). Interestingly, three Cu atoms and three P atoms can form a cyclic triangle coordination mode [76]. The coordination mode between N and Cu is somewhat similar to that between P and Cu, as one Cu atom can coordinate with one or two P atoms, and both N and P atoms can form the dimer mode of R–N(P)–Cu (Scheme 1c) [21, 35, 77, 78]. However, unlike P, one N atom cannot coordinate with two or more Cu atoms, but it can form the trimer mode of R–N–Cu, and a cyclic quadrangle mode of Cu_4N_4 is also available [77]. It is worth noting that, for S, N, P atoms, they coordinate with the Cu atom mainly through σ bonding, nevertheless, for alkynyl ligand, it can coordinate with Cu atom with either σ bonding or π bonding or both. As shown in Scheme 1d, one alkynyl ligand can not only coordinate with three or four Cu atoms with only σ bonding, but also can coordinate with two, three, or four Cu atoms with both σ bonding and π bonding [36, 37, 79, 80]. There are seven essential types of coordination modes: μ_2-η^1, η^2; μ_3-η^1, η^1, η^1; μ_3-η^1, η^1, η^2; μ_3-η^1, η^2, η^2; μ_4-η^1, η^1, η^1, η^1; μ_4-η^1, η^1, η^1, η^2; μ_4-η^1, η^1, η^2, η^2. Such unique binding modes can impart alkynyl-protected Cu nanoclusters with some drastically different physicochemical properties and functionalities from thiolate, nitrogen, and phosphine ligand stabilized Cu nanoclusters [72, 73].

2 Synthesis of Atomically Precise Cu Nanoclusters

There are various methods to synthesize bulky metal nanoparticles. However, preparing metal nanoclusters with atomic precision is still quite challenging. This is because metal nanoclusters with molecular purity typically form under specific thermodynamic or kinetic conditions. Since the pioneering Brust method to prepare thiolate-protected Au nanoclusters

https://doi.org/10.1007/s40820-024-01555-6

reported at 1990s [81, 82], a number of methods have been developed to prepare Au nanoclusters or Ag nanoclusters protected by thiolate, alkynyl molecule, and other ligands. The typical approaches include, but are not limited to, the direct reduction of the precursor, one-pot strategy, bi-phase method, ligand exchange or etching and so on [4, 83–87]. It is worth noting that, to prepare monodisperse metal nanoclusters, there are a lot of factors influencing the output, e.g., the reaction temperature, the solvent, the reducing agent, the nature and chemical property of the ligand molecule, the stoichiometric ratio of ligand–reductant–reactant, and so on. For instance, our group developed a synchronous nucleation and passivation strategy to synthesize alkynyl-protected coinage metal nanoclusters [88], and so far, several Au [88, 89], Ag [29, 32], AuAg [90–92], AgPd [93], AgRh [94, 95] nanoclusters have been successfully fabricated by this method [73, 96], but this approach is not applicable to thiolate-protected metal nanoclusters. Meanwhile, no successful case has been achieved on Cu nanoclusters yet. It also implies that, the approaches developed for synthesizing molecular thiolate-protected metal nanoclusters or alkynyl-protected metal (and alloy but not pure Cu) nanoclusters are not applicable for preparing atomically precise Cu nanoclusters, probably due to the different metal–ligand interactions can alter the nuclei growth and surface passivation behaviors [97].

Nevertheless, several generic methods have been developed for synthesizing monodisperses or molecular Cu nanoclusters. It includes the precursor reduction method, gradient reduction strategy (GRS), one-pot synthesis (OPS), ligand-exchange-induced growth, and other ingenious methods (Fig. 1). Each method has its own advantages or disadvantages. For example, the precursor reduction method is quite straightforward, but polydisperse cluster product may be acquired; the gradient reduction strategy features two step reduction with manipulation accessibility at each step, but the overall yield might be quite low; the one-pot synthesis holds facile operation but complex product is highly possible; the other methods are more applicable to special ligand to target specific cluster molecule. The advantages and disadvantages of these methods with specific cases will be elaborated next.

2.1 Precursor Reduction Method

The simplest and most straightforward method to fabricate Cu nanoclusters is to form the precursor first and then reduce it. However, under most circumstances, polydispersed Cu nanoclusters with a wide size distribution are acquired. To improve the monodispersity, kinetic control is inevitable. One typical example is the synthesis of $[Cu_{18}H_3(S\text{-}Adm)_{12}(PPh_3)_4Cl_2]$ molecule reported by Mandal group [42]. As shown in Scheme 2, $Cu(CH_3CN)_4BF_4$ was treated with auxiliary PPh_3 ligand first, and then the adamantanethiol (Adm-SH) ligand was added to form the Cu(I) complex. Upon the addition of the $NaBH_4$ methanol solution, the mixture changed from colorless into red, indicating the Cu_{18} nanocluster was formed. Note that, the employment of the bulky Adm-SH ligand is critical for yielding the Cu_{18} nanocluster here, as it acts as the main surface protecting ligand to stabilize the framework of the Cu_{18} nanocluster [42]. The Cu(I) precursor, also called as the Cu(I) complex, can be prepared step by step. In 2020, Li et al. reported a copper hydride cluster of $[Cu_{32}(PET)_{24}H_8Cl_2](PPh_4)_2$ (PET = phenylethyl thiolate) [39]. For its synthesis, Cu(TMEDA)Cl (TMEDA: tetramethylethylenediamine) was first obtained by reacting CuCl with TMEDA. Upon addition of PPh_4Br and the thiol ligand (PETH), the final stage precursor of CuPET(TMEDA)Cl was obtained. The reduction of CuPET(TMEDA)Cl by sodium borohydride can yield Cu_{32} nanoclusters [39]. In 2023, Jia et al. utilized this method to fabricate an eight-electron superatom of $[Cu_{31}(4\text{-}MeO\text{-}PhC{\equiv}C)_{21}(dppe)_3](ClO_4)_2$ (Cu_{31}, dppe = 1, 2-bis(diphenylphosphino)ethane) cluster [43]. Specifically, $Cu(ClO_4)_2{\cdot}6H_2O$ reacts with 4-methoxyphenylacetylene and dppe in the presence of triethylamine to form the precursor first, then Cu_{31} nanoclusters were obtained upon the reduction of borohydride [43]. Interestingly, side product of $[Cu_6(4\text{-}MeO\text{-}PhC{\equiv}C)_5(dppe)_3](ClO_4)$ (it is a Cu(I) cluster not a superatom) was also isolated from the obtained single crystals of the Cu_{31} nanoclusters [44]. Recently, Fang, Wei and Shen et al. documented the fabrication of four Cu_{50} clusters with nearly identical metal frameworks [45]. Using $Cu_{50}(CF_3COO)_{12}(3, 5\text{-}di\text{Me-PhS})_{18}(PPh_3)_4H_2$ (Cu_{50}-1) as an example, $Cu(CF_3COO)_2$ was first prepared as the Cu source, and after it reacted with 3, 5-dimethylbenzenethiol and PPh_3, $NaBH_4$ was added as a reducing agent to obtain the raw cluster product [45].

It is worth noting that, after forming the raw product by the precursor reduction method, adding some auxiliary ligand to etch the clusters may help to improve the yield and stability of the final product. For instance, Shen and coworkers

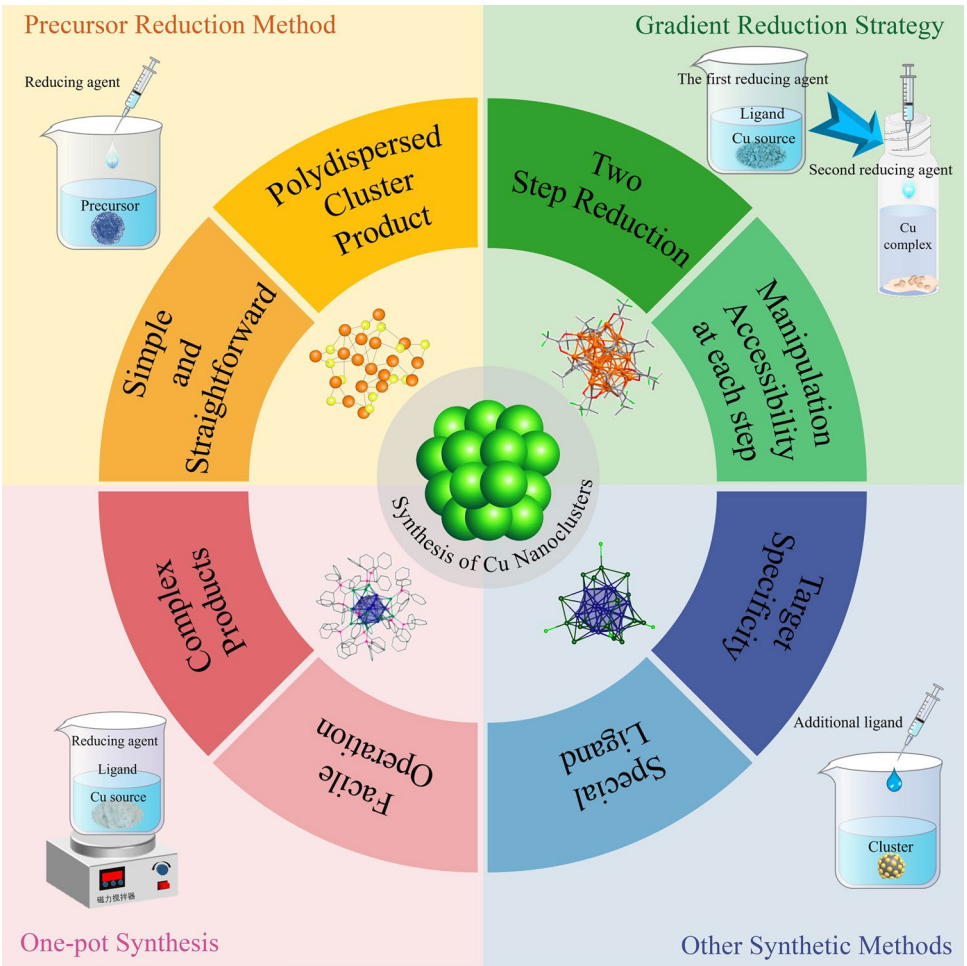

Fig. 1 Current synthetic methods for atomically precise Cu nanoclusters

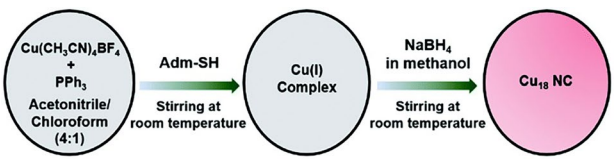

Scheme 2 Synthetic route of Cu_{18} nanoclusters. Reproduced with permission from Ref. [42], Copyright 2022 Royal Society of Chemistry

recently reported a couple of "isostructural" Cu clusters of $[Cu_{41}Cl_2(2\text{-F-}C_6H_4S)_{12}(CF_3COO)_6(PPh_3)_6H_{19}]^{2-}$ and $[Cu_{41}(2, 5\text{-di-Methyl-}C_6H_3S)_{12}(BO_3)_3Cl_3(PPh_3)_6H_{19}]$ [46]. The raw product was formed by reacting $Cu(CF_3COO)_2$ with 2-fluorothiophenol and PPh_3 ligand, but after that, additional PPh_3Cl ligand was added to introduce Cl onto the two Cu_{41} clusters for enhanced stability [46].

2.2 Gradient Reduction Strategy (GRS)

The gradient reduction strategy was first employed by the Zheng group to synthesize Cu_{53} nanoclusters, but the method was not named then in 2019 [48]. Specifically, $Cu(CF_3COO)_2$ was first reduced by Cu powder, after the tert-butylacetylene ($HC{\equiv}C^tBu$) ligand was added, $PhSiH_2$ as the second reducing agent was introduced into the solution under vigorous stirring. It is believed that the cooperation between Cu powder and $PhSiH_2$ contributed together to achieve the high-nuclearity Cu(I)/Cu(0) cluster of $[Cu_{53}(RCOO)_{10}(C{\equiv}C^tBu)_{20}Cl_2H_{18}]^+$ [48]. In another study, the synthesis and overall structure of $Cu_{53}(C{\equiv}CPhPh)_9(dppp)_6Cl_3(NO_3)_9$ nanocluster was recorded by Li and Zhang group. In a typical trial, 4-ethynylbiphenyl (BP) and 1, 3-bis(diphenylphosphino)propane

 https://doi.org/10.1007/s40820-024-01555-6

(dppp) were sequentially added into an ethanol solution of $Cu(NO_3)_2$, then $NaBH_4$ was introduced, followed by aging the reaction to obtain the target cluster [37].

In 2020, the name of gradient reduction strategy was formally proposed by Sun group [47]. In this method, the valence of the Cu atom evolved from +2 to +1, then to 0 by using different reducing agents at different stages. As illustrated in Scheme 3, the comproportionation of Cu(II) and Cu powder can yield the Cu(I) complex first, then the Cu(I) complex was further reduced to generate $[Cu_{23}(^tBuC{\equiv}C)_{13}(CF_3COO)_6]$ (SD/Cu23a) or $[Cu_{23}(^tBuC{\equiv}C)_{13}(CF_3COO)_6]{\cdot}CHCl_3$ (SD/Cu23b). Such method showed the solvent-dependent polymorphism. It is worth noting that the Cu_{23} nanoclusters are superatoms, not Cu(I) complex, and both of them have four valent electrons. They also contain a very rare $[Cu_4]^0$ kernel surrounded by an outer Cu_{19} shell. In addition, depending on the solvent, the Cu_{23} nanocluster can crystallize into two polymorphs [47]. In 2022, the same group conducted the synthesis of two quasi-structurally isomeric 13-nuclei Cu nanoclusters (Cu13a and Cu13b) by the GRS method in a similar manner [49]. In this study, after the reaction of Cu(II) and CZ-PrAH (9-(prop-2-yn-1-yl)-9H-carbazole) with Cu powder to yield a yellow Cu(I) intermediate, the ligand was added into the mixture, following that a freshly prepared ethanol solution of $NaBH_4$ was added under vigorous stirring. The reducing agent of $NaBH_4$ with strong reducing capability was employed to avoid the re-oxidation of Cu(I) species [49]. Recently, Li et al. reported the comprehensive characterization and electrocatalytic CO_2 reduction of $[Cu_{26}(DPPE)_3(CF_3CO_2)_8(CH_3O)_2(^tBuC{\equiv}C)_4H_{11}]^+$, which was also synthesized by this GRS approach [38].

2.3 One-Pot Synthesis (OPS)

Compared to the above two methods, one-pot synthesis is the most facile method to operate, as it does not require to form the Cu(I) precursor. Basically, all the reactants including the Cu salt, the ligand molecules, the reducing agent and the base are mixed to generate the Cu nanoclusters. Of course, the Cu(I) precursor is formed in the reaction system, but no isolation is necessary. It is known that such method has been employed for synthesizing quite a number of coinage metal

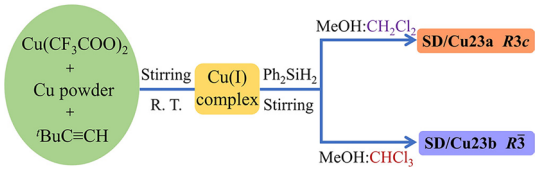

Scheme 3 Synthetic route of Cu23a and Cu23b nanoclusters by GRS. Reproduced with permission from Ref. [47], Copyright 2020 American Chemical Society

nanoclusters, e.g., thiolate Au_{25} nanoclusters can be easily prepared by one-pot approach [98, 99], the Tsukuda group fabricated a series of alkynyl-protected Au_{22} clusters by this method [100], and the Wang group reported the preparation of $Au_{23}(C{\equiv}CR)_{15}$ through one-pot synthesis as well [101].

It is worth noting that making Cu superatom cluster is rather different from making Au and Ag superatoms, as Cu(I) is more resistant to reduction. Therefore, in the presence of hydride source, a reduction can easily yield Au or Ag superatoms [2, 102], but Cu(I)-hydride complex is usually formed. It is more difficult to observe Cu(0) clusters, mainly due to the higher stability of Cu(I)-hydride complex than Au(I)-hydride or Ag(I)-hydride complexes. However, in a ligand-deficient environment, the reduction of Cu(I)-hydride complex might generate some unstable $(CuH)_x$ species that are amenable for cluster growth. In 2015, the Scott and Hayton group recorded the synthesis of $[Cu_{25}H_{22}(PPh_3)_{12}]Cl$ and $[Cu_{18}H_{17}(PPh_3)_{10}]Cl$ by this method [40]. As summarized in Scheme 4, adding 13 equiv. of Ph_2SiH_2 to a slurry containing 24 equiv. of Cu(OAc), 12 equiv. of PPh_3, and 1 equiv. of CuCl in C_6H_6 can result in a rapid color change from pale green to dark red then into deep green, concomitant with the precipitation of a dark brown solid after keeping stirring in 24 h. Two clusters of $[Cu_{25}H_{22}(PPh_3)_{12}]Cl$ and $[Cu_{18}H_{17}(PPh_3)_{10}]Cl$ were isolated with a yield of 23% and 14%, respectively [40]. Following this study, the same group accomplished the synthesis of $[Cu_{20}(C{\equiv}CPh)_{12}(OAc)_6)]$ by the same approach [36].

2.4 Other Synthetic Methods

Besides the above approaches, researchers have developed several other ingenious methods to prepare atomically precise Cu nanoclusters. In 2016, the Hayton group reported a ligand-exchange-induced growth from a smaller cluster to

synthesize Cu_{29} nanoclusters [35]. As shown in Scheme 5, $[Cu_{25}H_{22}(PPh_3)_{12}]Cl$ was first synthesized, and then the addition of 16 equiv of 4, 7-diphenyl-1, 10-phenanthroline (Ph_2phen) can cause an immediate color change from dark green to dark blue, and workup of this mixture for 15 min resulted in the isolation of $[Cu_{29}Cl_4H_{22}(Ph_2phen)_{12}]Cl$, a deep blue black crystalline material in a yield of 84%. Meanwhile, the reaction of $[Cu_{25}H_{22}(PPh_3)_{12}]Cl$ with 1, 10-phenanthroline also yielded a deep blue molecule, which is probably the isostructural molecule of $[Cu_{29}Cl_4H_{22}(Ph_2phen)_{12}]Cl$, but no single crystal XRD data were available to confirm that [35].

Note that the introduction of additional ligand does not necessarily lead to cluster growth or size expansion; instead, cluster size decrease is also possible. Chakrahari et al. reported the $[Cu_{13}(S_2CN^nBu_2)_6(C{\equiv}CR)_4](PF_6)$ (R=C(O)OMe, C_6H_4F) cluster which was synthesized through size transformation (Scheme 6) [103]. As the hydride in $[Cu_{28}H_{15}(S_2CN^nBu_2)_{12}]^+$ is substantially hydridic, the terminal alkyne is sufficiently acidic enough to react with it to yield $[Cu_{13}(S_2CN^nBu_2)_6(C{\equiv}CR)_4]^+$, which features a centered cuboctahedral $[Cu_{13}]^{11+}$ core with two free electrons, and $[Cu_8H(S_2CN^nBu_2)_6(C{\equiv}CR)_4]^+$ was also isolated as the side product [103].

Scheme 4 Synthetic route of Cu_{25} and Cu_{28} nanoclusters. Reproduced with permission from Ref. [40], Copyright 2015 American Chemical Society

3 Atomically Precise Cu Nanoclusters for Catalytic Applications

Thanks to the precise composition and structure of Cu nanoclusters, they can serve as ideal model catalysts for a variety of reactions [50]. Also, theoretical simulations can build precise models to reveal the reaction pathway and help to elucidate the reaction mechanism [104, 105]. In line with this, a great deal of research effort has been devoted to exploring the catalytic applications of atomically precise Cu nanoclusters, including but not limited to electrocatalytic reactions, photocatalytic reactions, organic reactions, as well as other catalytic processes (Fig. 2).

3.1 Cu NCs for Electrocatalysis

The electrocatalysis technology has drawn widespread attention and found immerse values in a wide spectrum of

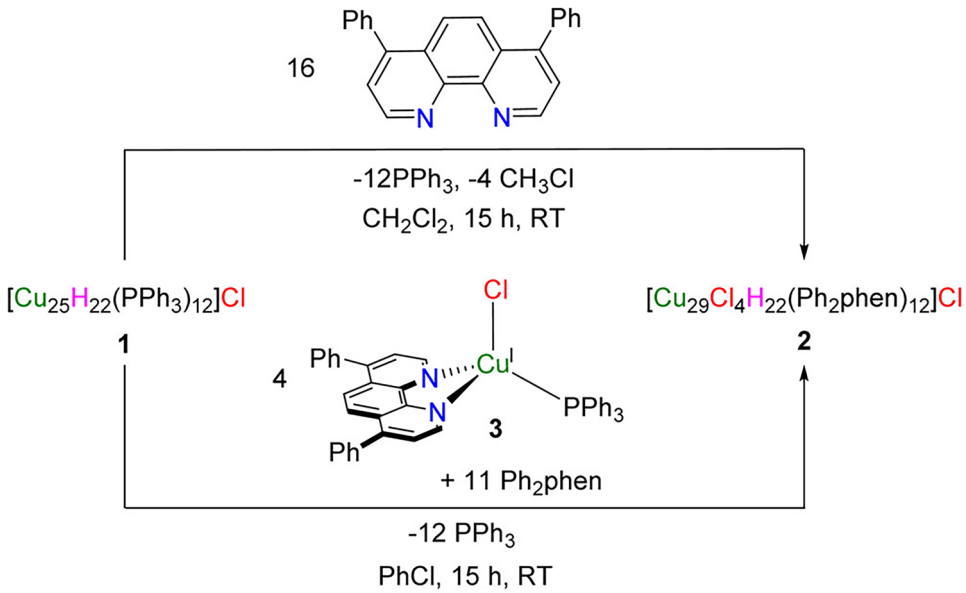

Scheme 5 Two cluster expansion synthetic routes for Cu_{29} nanoclusters. Reproduced with permission from Ref. [35], Copyright 2016 American Chemical Society

https://doi.org/10.1007/s40820-024-01555-6

fields especially in green energy storage and conversion, as electrocatalysis is not only highly efficient, mild condition operational, multifunctional, but also can couple with renewable intermittent energy sources such as solar, wind, and geothermal energy [106]. Therefore, electrocatalysis represents a sustainable strategy to address global environmental pollution and heavy reliance on fossil fuels [107].

In the last decade, the fast industrialization and huge demand for fossil fuels have caused a dramatic worldwide increase of CO_2 emission, which is the main culprit of global warming. However, CO_2 is an abundant source that can be used as substrate to fabricate various valuable products such formic acid, formamide, urea, and other hydrocarbon compounds [108, 109]. Electrochemical CO_2 reduction reaction (eCO_2RR) can realize such conversion with high efficiency and in an environmentally friendly manner; however, due to the chemical inertness and thermodynamic stability of linear CO_2 molecules, a prerequisite for achieving CO_2 reduction lies in finding a catalyst that can lower the chemical energy required to break the C-O bond [110, 111]. Moreover, eCO_2RR involves multiple electron transfer, and various products including C1 compounds (e.g., CO, HCO_2H, CH_3OH) and C2 compounds (e.g., CH_3CO_2H, CH_3CHO, C_2H_4, C_2H_6, etc.) can be generated. The thermodynamic potentials, various reactions, and corresponding products are summarized in Table 2 [112]. It can be noted that different reactions occur at very similar thermodynamic equilibrium potentials, plus the competing hydrogen evolution reaction (HER), it is extremely challenging to achieve highly selective CO_2 reduction product. Therefore, designing efficient, durable, and high-selectivity catalysts for eCO_2RR to acquire target product is highly desired [113].

So far, all kinds of nanostructured materials including metal oxides, metal alloys, carbon substrates, two-dimensional nanomaterials have been investigated as catalysts for eCO_2RR [114–118]. Among a series of metal-based catalysts, Cu nanomaterials are one of the most promising catalysts that can deep electrochemically reduce CO_2 into valuable chemicals, especially hydrocarbon products [119–122]. However, for most Cu-based catalysts, the chemical nature is not uniform, e.g., no homogeneous size, shape, architecture, and structure hence it is extremely challenging to ascertain the chemical nature of the catalyst and eventually establish the structure–activity relationship [123–125]. Recently, molecular Cu nanoclusters have been drawing attention from the heterogeneous catalysis field, thanks to the high surface-to-volume ratio, strong binding capability to the key reaction intermediates, and more importantly, the atomically precise crystallographic structure and well-defined architecture [50, 90, 126].

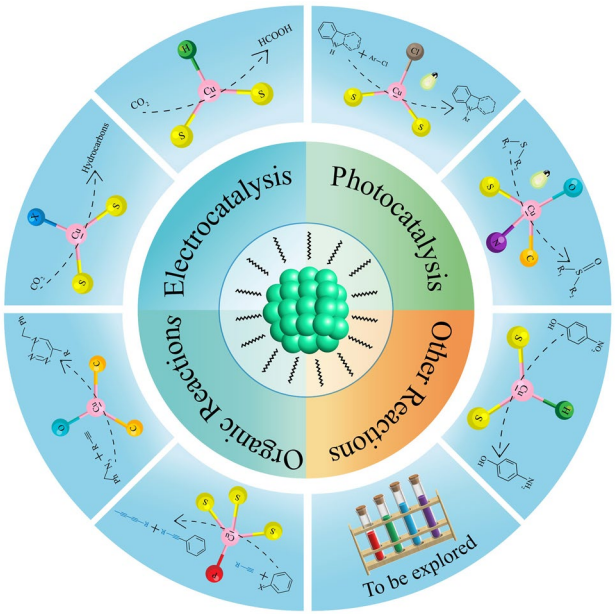

Fig. 2 Catalytic applications of atomically precise Cu nanoclusters

In 2017, Tang et al. reported a structurally precise Cu–hydride nanocluster of $Cu_{32}H_{20}L_{12}$ (L is a dithiophosphate ligand), which offered unique selectivity for eCO_2RR at low overpotentials [51]. By density functional theory calculations, the authors first predicted that the presence of negatively charged hydride in Cu nanocluster plays a crucial role in determining the selectivity of the

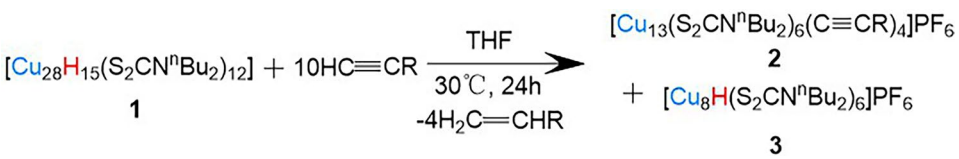

Scheme 6 Synthesis of $[Cu_{13}(S_2CN^nBu_2)_6(C{\equiv}CR)_4](PF_6)$ cluster. Reproduced with permission from Ref. [103], Copyright 2016 Wiley VCH

Table 2 Electrochemical CO_2 reduction reactions yielding various products with thermodynamic equilibrium potentials in an aqueous electrolyte at pH 7, 1 atm, and 25 °C, relative to the reversible hydrogen electrode (RHE)

Reactions	E_0 (V *vs.* RHE)	Product
$CO_2 + 2H^+ + 2e^- \rightarrow CO_{(g)} + H_2O$	−0.11	Carbon monoxide
$CO_2 + 2H^+ + 2e^- \rightarrow HCOOH_{(aq)}$	−0.12	Formic acid
$CO_2 + 6H^+ + 6e^- \rightarrow CH_3OH_{(aq)} + H_2O$	0.03	Methanol
$CO_2 + 8H^+ + 8e^- \rightarrow CH_{4\,(g)} + 2H_2O$	0.17	Methane
$2CO_2 + 10H^+ + 10e^- \rightarrow CH_3CHO_{(aq)} + 3H_2O$	0.06	Acetaldehyde
$2CO_2 + 12H^+ + 12e^- \rightarrow C_2H_{4\,(aq)} + 4H_2O$	0.08	Ethylene
$2CO_2 + 12H^+ + 12e^- \rightarrow C_2H_5OH_{(aq)} + 3H_2O$	0.09	Ethanol
$2CO_2 + 14H^+ + 14e^- \rightarrow C_2H_{6\,(aq)} + 4H_2O$	0.14	Ethane
$2CO_2 + 16H^+ + 16e^- \rightarrow C_2H_5CHO_{(aq)} + 5H_2O$	0.09	Propionaldehyde
$3CO_2 + 18H^+ + 18e^- \rightarrow C_3H_7OH_{(aq)} + 5H_2O$	0.1	Propanol
$2H^+ + 2e^- \rightarrow H_2$	0	Hydrogen evolution reaction
$2H_2O \rightarrow O_2 + 4H^+ + 4e^-$	1.23	Oxygen evolution reaction

products, yielding HCO_2H over CO at lower overpotentials. The optimized structure of the $Cu_{32}H_{20}L_{12}$ cluster is shown in Fig. 3a, and the Cu_{32} cluster has a distorted 14-Cu-atom formed hexacapped rhombohedral core sandwiched between two 9-Cu-atom formed triangular cupola fragments. Meanwhile, the 20 hydrides are divided into 12 triply coordinated H (μ_3-H), 6 tetra-coordinated H (μ_4-H), and 2 penta-coordinated H (μ_5-H). For CO_2 reduction into CO on the $Cu_{32}H_{20}L_{12}$ cluster, it adopts either the proton-reduction channel or lattice-hydride mechanism (Fig. 3b). It can be clearly noted that the lattice hydride pathway is more favorable, where the rate-determining step is the μ_3-H1 hydride being transferred to form the $Cu_{32}H_{19}L_{12}$-HCOO intermediate with a free energy change of 0.32 eV (Fig. 3b right). In contrast, the formation of $Cu_{32}H_{19}L_{12}$-HCOO in the proton reduction channel requires an energy gap of 1.08 eV (Fig. 3b left). Finally, the authors conducted the eCO_2RR test of the $Cu_{32}H_{20}L_{12}$ cluster to verify the theoretical predictions. As shown in Fig. 3c, the average current density becomes significant at the overpotential of 0.3 V and increases with the increasing of the overpotential. H_2, CO, and HCOOH are the main products, and the cumulative Faradaic efficiency (FE) is over 90%. The product selectivity is illustrated in Fig. 3d. HCO_2H is the predominant major product in the overpotential window from 0.3 to 0.4 V, and HER dominates at higher overpotentials (from 0.5 to 0.6 V) [51]. These experimental results confirmed the theoretical predictions, and this study showcases that the hydride-containing Cu nanoclusters may offer a unique product selectivity over conventional transition metal nanocatalysts for eCO_2RR.

Furthermore, the core configuration of Cu nanoclusters can be manipulated to further mediate the activity and selectivity of eCO_2RR. In 2022, the Zang and Wang group reported three novel isomeric Cu_8-cluster with cores composed of two types of metal kernels (ditetrahedral vs. cubic) and studied the morphological kernel influence on the electrochemical eCO_2RR at the atomic level [52]. Specifically, three Cu clusters of $Cu_8(H)$-$(L1)_6PF_6$, $Cu_8(^t BuS)_4(L1)_4$, and $Cu_8(^t BuS)_4(L2)_4$ (Cu_8-1, Cu_8-2, and Cu_8-3, respectively, where L1 = 9*H*-carbazole-9-carbodithioate and L2 = *O*-ethyl carbonodithiolate) were prepared, and the total structures are illustrated in Fig. 4a–c. Cu_8-1 contains a slightly twisted cubic Cu_8^{8+} core, while Cu_8-2 and Cu_8-3 show the identical di-tetrahedral configurations. In eCO_2RR test, H_2, CO, and HCO_2H were the main products, and the total FE values were over 90% (Fig. 4d). Moreover, the di-tetrahedron-shaped Cu_8 clusters (Cu_8-2 and Cu_8-3) exhibited a higher $FEHCOH_2$ and greater selectivity than the cube-shaped Cu_8 cluster (Cu_8-1), where Cu_8-2 demonstrated remarkable HCO_2H selectivity, manifested by the $FEHCO_2H$ values of 90% and 92% at −0.9 and −1.0 V, respectively (Fig. 4d). Meanwhile, in the long-term stability test of 8 h, only the current density from Cu_8-2 remained almost unchanged, indicating robust durability for prolonged operation (Fig. 4e). At last, the free energies of each step for Cu_8-1 and Cu_8-2 were calculated. Noteworthily, for the adsorbed $*CO_2$ being converted into HCOO*, the di-tetrahedron-shaped Cu_8-2 cluster (−0.91 eV) has a much lower free energy than the cube-shaped Cu_8-1 cluster

https://doi.org/10.1007/s40820-024-01555-6

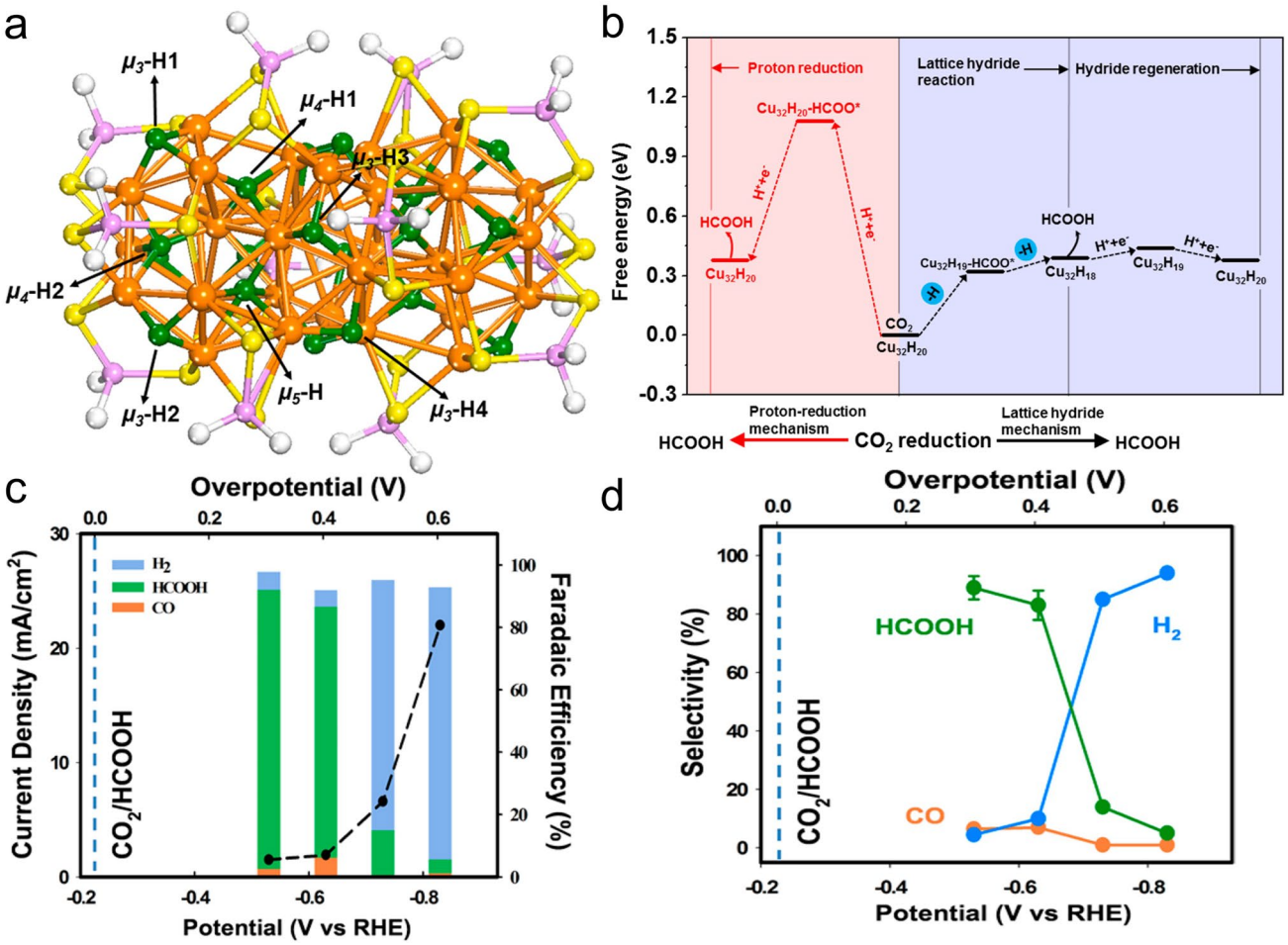

Fig. 3 **a** Total structure of $Cu_{32}H_{20}L_{12}$ nanocluster. Color codes: Cu (orange), S (yellow), hydride (green), H (white), P (purple). **b** CO_2 electroreduction on $Cu_{32}H_{20}L_{12}$ to form HCOOH via the proton-reduction channel (left) and the lattice-hydride channel (right). **c** Average current densities (black circles) and cumulative Faradaic efficiencies (stacked bars) obtained at different overpotentials. **d** Product selectivity for H_2, HCOOH, and CO at different overpotentials. Reproduced with permission from Ref. [51], Copyright 2017 American Chemical Society

(−0.23 eV). Since the rate determining step is the formation of COOH* to generate HCO_2H, the Cu_8-2 cluster is more favorable for HCO_2H production [52]. This investigation showcases the modulation of activity and selectivity toward CO_2 electroreduction by tailoring the Cu core, which can probably trigger more endeavors to design tailored Cu based catalysts for eCO_2RR.

It is worth noting that for most reported atomically precise Cu nanoclusters in the eCO_2RR, C1 products of CO and HCO_2H with high selectivity are normally obtained. This is probably due to the Cu active sites are coordination symmetric (typically CuS_3). Compared to the C1 products of CO/HCO_2H, the high energy density hydrocarbon products such as CH_4 and C_2H_4 are highly sought as potential fuels [127–130]. To switch the C1 products to more valuable hydrocarbons, Wu et al. recently reported a catalyst based Cu_6 nanocluster with symmetry-broken CuS_2N_1 active sites [27]. The total structure of the as-prepared $Cu_6(MBD)_6$ nanocluster (MBD = 2-mercaptobenzimidazole) is shown in Fig. 5a. Each MBD ligand has the tridentate sites to coordinate three Cu atoms, where the thiolate S atom binds with two Cu atoms and the N atom binds to the other Cu atom (Fig. 5b). Meanwhile, each Cu atom is coordinated by two S atoms and one N atom (Fig. 5c). It is symmetry-broken distorted CuS_2N_1 geometry, as the bonding length values are all different ($Cu_1-S_1 = 2.2118$ A, $Cu_1-S_{1a} = 2.2924$ A, $Cu_1-N_1 = 1.9757$ A). In addition, six Cu atoms formed a distorted octahedron with the Cu–Cu bonding ranging

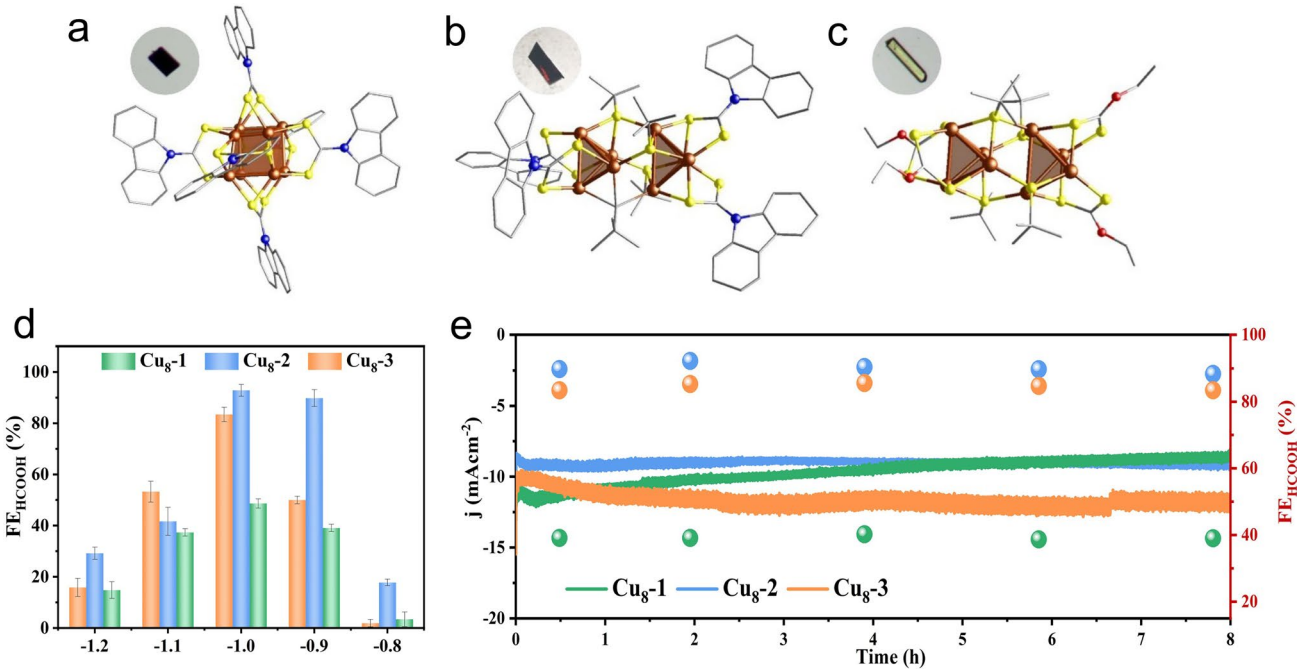

Fig. 4 The total structures of **a** Cu_8-1, **b** Cu_8-2, and **c** Cu_8-3. Color codes: Cu (brown), S (yellow), C (gray), O (red), N (blue). Electrocatalytic performances of **d** FE_{HCOOH} of Cu_8-1, Cu_8-2, and Cu_8-3 at different applied potentials. **e** Stability tests of the catalysts for eCO_2RR (Cu_8-1 and Cu_8-2 at -0.9 V, Cu_8-3 at −1.0 V). Reproduced with permission from Ref. [52], Copyright 2022 Wiley VCH

from 3.083 to 3.254 Å, which might be favorable for C–C coupling (Fig. 5d). There is sufficient space above the distorted CuS_2N_1 geometry, which can be accessible for CO_2 adsorption (Fig. 5e). When using $Cu_6(MBD)_6$ nanocluster as the catalyst, the product distribution is shown in Fig. 5f. When the potential goes from −0.7 to −1.4 V, the FE_{CO} and FE_{H2} gradually decreased; meanwhile, the FEC_2H_4 and FEC_2H_4 gradually increased (Fig. 5f). The highest FE_{CH4} reached 42.5% at −1.4 V with a large partial current density of −119.0 mA cm^{-2}, with the FEC_2H_4 of 23.0% and the partial current density of −64.4 mA cm^{-2} (Fig. 5g). That is, in a wide potential window, CH_4 and C_2H_4 are the dominant products rather than CO. To gain more insights into the advantages of symmetry-breaking at the catalytic sites, in situ Cu K-edge XANES measurement of $Cu_6(MBD)_6$ was conducted, revealing that there is clear electron transfer from $Cu_6(MBD)_6$ to the CO_2 molecule. Thus, the $Cu_6(MBD)_6$ cluster with asymmetric CuS_2N_1 sites has a better CO_2 activation capacity than the $Cu_8(^tBuS)_4(L2)_4$ cluster with the symmetric CuS_3 sites. The integrated projected density of states (IPDOS) of Cu sites in $Cu_6(MBD)_6$ and $Cu_8(^tBuS)_4(L2)_4$ were then calculated. For $Cu_6(MBD)_6$, the d_{x2-y2} orbital of Cu-S_2N_1 site has the highest number of electrons close to the Fermi energy level (Fig. 5h), whereas the highest d orbital is Cu d_{xz} in CuS_3 sites of $Cu_8(^tBuS)_4(L2)_4$ (Fig. 5i). It suggests that the coordination-symmetry breaking significantly affects the highest occupied d-orbital, which plays a critical role in regulating the coordination mode of the reactant and intermediate. When the C atom of CO_2 is adsorbed onto the $Cu_6(MBD)_6$, the highest occupied d_{x2-y2} orbital can energy-match with the lowest occupied π^* orbital of CO_2 to form a π-complex rather than the conventional σ-complex, where the π-complex can lower the energy barrier of CO_2 activation. If the O atom of CO_2 is adsorbed onto the $Cu_6(MBD)_6$, a σ-complex is formed, and for $Cu_8(^tBuS)_4(L2)_4$, a π-complex is formed only when the O atom in CO_2 is the adsorbed atom. Consequently, due to superiority of the C atom adsorbing on $Cu_6(MBD)_6$, the hydrogenation on the less hindered O atom to form the key *COOH intermediate rather than the *OCHO intermediate is more favorable, making the reaction proceed to yield the CH_4/C_2H_4 products [27]. This study highlights the importance of regulating the coordination mode of Cu nanoclusters, which might be a promising direction for designing

https://doi.org/10.1007/s40820-024-01555-6

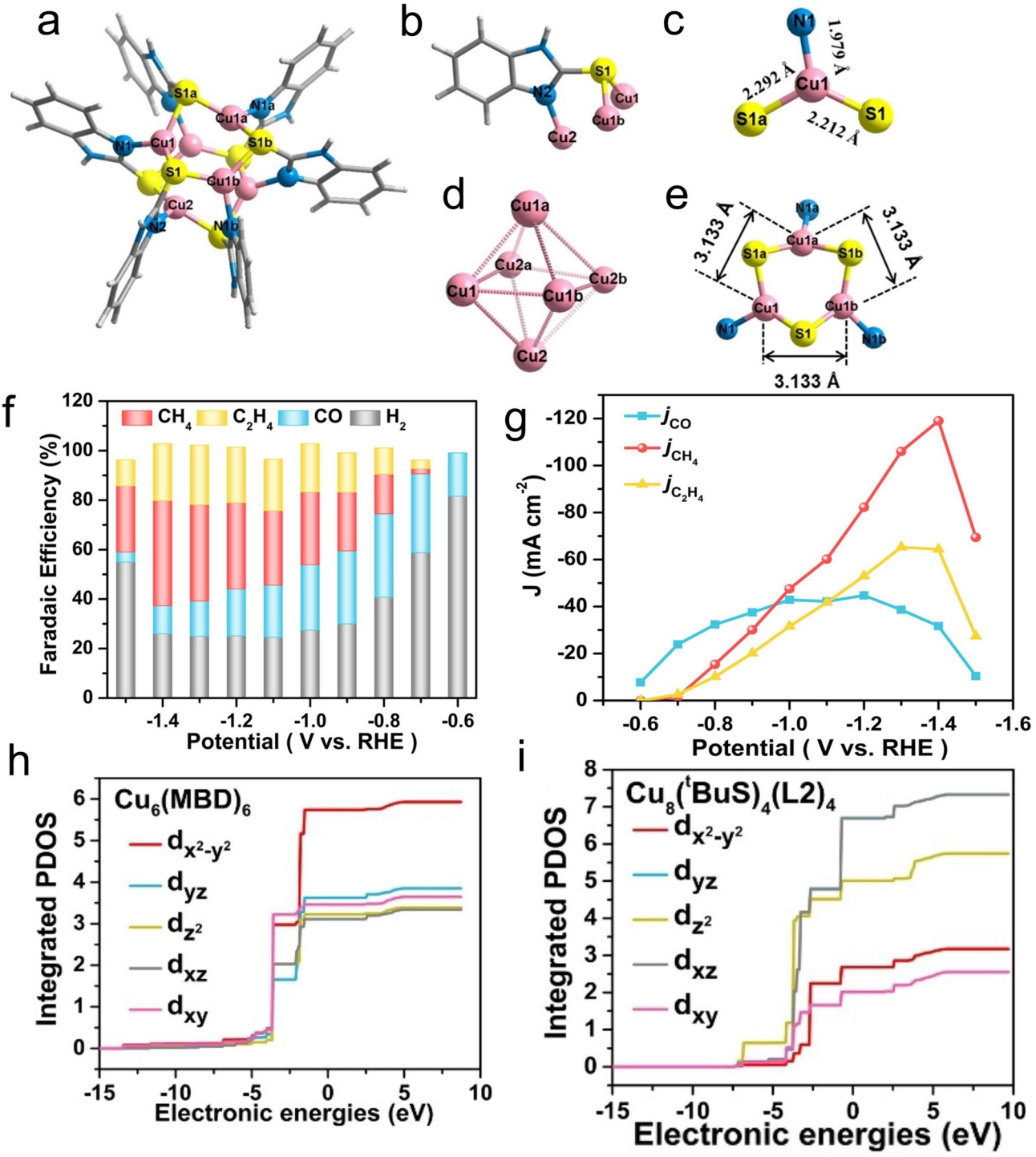

Fig. 5 **a–e** Structural analysis of $Cu_6(MBD)_6$ nanocluster. Color codes: pink, Cu; blue, N; yellow, S; deep gray, C; light gray, H. **f** FEs of CH_4, C_2H_4, CO and H_2 at different potential on $Cu_6(MBD)_6$. **g** Partial current densities of CH_4, C_2H_4, and CO on $Cu_6(MBD)_6$. IPDOS of 3d orbitals: d-density of states vs. the Fermi level projected onto Cu atoms in (**h**) $Cu_6(MBD)_6$ and (**i**) $Cu_8(^tBuS)_4(L2)_4$. Reproduced with permission from Ref. [27], Copyright 2023 Wiley VCH

metal nanoclusters as highly efficient CO_2 reduction electrocatalysts toward valuable hydrocarbon production.

The large surface area, good catalytic activity and strong capability to suppress HER also enable Cu nanoclusters as potent catalysts for electrochemical nitrate reduction reaction (eNO_3RR) [131, 132], a process that can turn nitrate contaminant into valuable NH_3 product. Specifically, NH_3 is an important feedstock for preparing nitrogen-containing fertilizer, pharmaceuticals, chemicals, and agricultural products, and it is also a valuable green energy carrier [133, 134]. However, the current global production of NH_3 is largely relying on the energy-intensive and large CO_2-emissive Haber–Bosch process. The electrochemical N_2 reduction powered by renewable energy offers a promising approach but it is significantly restricted by the low solubility of N_2 in water and the extremely high energy required to break the N≡N bond (941 kJ mol^{-1}). In stark contrast, nitrate is one of the major contaminants in wastewater and also has much weaker N–O bonding energy (250 kJ mol^{-1}). Therefore, developing efficient and stable electrocatalysts for NO_3RR is imperative for offering a sustainable strategy to produce NH_3 [135–138]. Recently, atomically precise metal nanoclusters have demonstrated great potential for catalyzing eNO_3RR, mainly thanks to the strong catalytic capability, and more importantly, the atomic precise structure can provide an ideal model to elucidate the complicated reaction pathway and establish the structure–activity correlation [131, 132, 139]. For instance, our group found that $Ag_{30}Pd_4(C_6H_9)_{26}](BPh_4)_2$ nanocluster can achieve the Faradaic efficiency of NH_3 over 90% in eNO_3RR, where the Ag site is responsible for converting NO_3^- into NO_2^- and the Pd site makes the major contribution to catalyze NO_2^- into NH_3 hence the whole reaction adopted a tandem catalytic mechanism [93].

Recently, Wang and Zang et al. utilized bulky carborane-alkynyl ligand to prepare atom-precise monomer $Cu_{13}{\cdot}3PF_6$ and bridged dimer $Cu_{26}{\cdot}4PF_6$ clusters, and both clusters exhibited remarkable catalytic activity and selectivity in eNO_3RR [53]. As illustrated in Fig. 6a, $Cu_{13}{\cdot}3PF_6$ has a metal skeleton, which could be viewed as two pentagonal bipyramids merged by sharing one equatorial edge but with one vertex of the pentagonal bipyramid being lost. $Cu_{26}{\cdot}4PF_6$ is a dimer of $Cu_{13}{\cdot}3PF_6$. To be specific, in $Cu_{26}{\cdot}4PF_6$, each Cu_{13} monomer loses a carbocycloalkynyl ligand and the adjacent PPh_3, and the vacated space is occupied by the nido-carboranealkynyl ligands unit of the other monomer via cyclopentadienyl anionic coordination (Fig. 6b). Interestingly, both clusters have fair stability and accessible open metal sites for eNO_3RR, where eNO_3RR was carried out in an H-type cell containing 0.1 M KNO_3 in 0.5 M K_2SO_4 medium (Fig. 6c). When the applied potential goes more negatively, the $FENH_3$ exhibited a volcano-shape change, and both clusters reached the maximal value at -0.85 V (vs. RHE). The maximal $FENH_3$ of $Cu_{26}{\cdot}4PF_6$ is 85.1%, much higher than that of $Cu_{13}{\cdot}3PF_6$. Meanwhile, at each measured potential, the FE and yield rate of NH_3 for $Cu_{26}{\cdot}4PF_6$ surpass that of $Cu_{13}{\cdot}3PF_6$ (Fig. 6d, e), despite the NH_3 yield rate increasing with the increasing of the applied potential (Fig. 6e). Finally, the authors elucidated the reaction pathway and mechanism with the aid of theoretical simulations and in-situ FTIR spectroscopic study. The free energy diagram in Fig. 6f suggests that $Cu_{13}{\cdot}3PF_6$ and $Cu_{26}{\cdot}4PF_6$ share the identical reaction pathway ($*NO_3 \rightarrow *NO_2 \rightarrow *NO \rightarrow *NHO \rightarrow *NH_2O \rightarrow *NH_2OH \rightarrow *NH_2 \rightarrow *NH_3$). For both clusters, the rate determining step (RDS) is identified as *NHO-to-$*NH_2O$, and the energy consumption for $Cu_{26}{\cdot}4PF_6$ is much lower than that of $Cu_{13}{\cdot}3PF_6$ (0.27 vs. 0.58 eV), indicating $Cu_{26}{\cdot}4PF_6$ is more energetically favorable for eNO_3RR. Moreover, the subsequent $*NH_2O$-to-$*NH_3$ reduction step is also a downhill process, demonstrating a strong interaction between the key intermediates and the active sites, which can promote the electron transfer and the following hydrogenation steps to accelerate the eNO_3RR process. This study not only establishes a platform to disclose the structure–activity relationship of Cu nanoclusters for eNO_3RR, but also provides a feasible strategy to access desirable Cu nanoclusters as efficient eNO_3RR catalysts [53].

3.2 Cu NCs for Photocatalysis

Solar energy is an inexhaustible natural energy source, and photocatalytic technology can utilize solar energy to realize environmental decontamination and energy conversion, particularly, photocatalytic technology can reduce CO_2 into valuable hydrocarbon fuels [140, 141]. The principle of photocatalytic reduction of CO_2 is to use photoexcited semiconductor photocatalysts to produce photogenerated electrons and holes, and the carriers take redox reactions on the surface of the catalyst, reducing

 https://doi.org/10.1007/s40820-024-01555-6

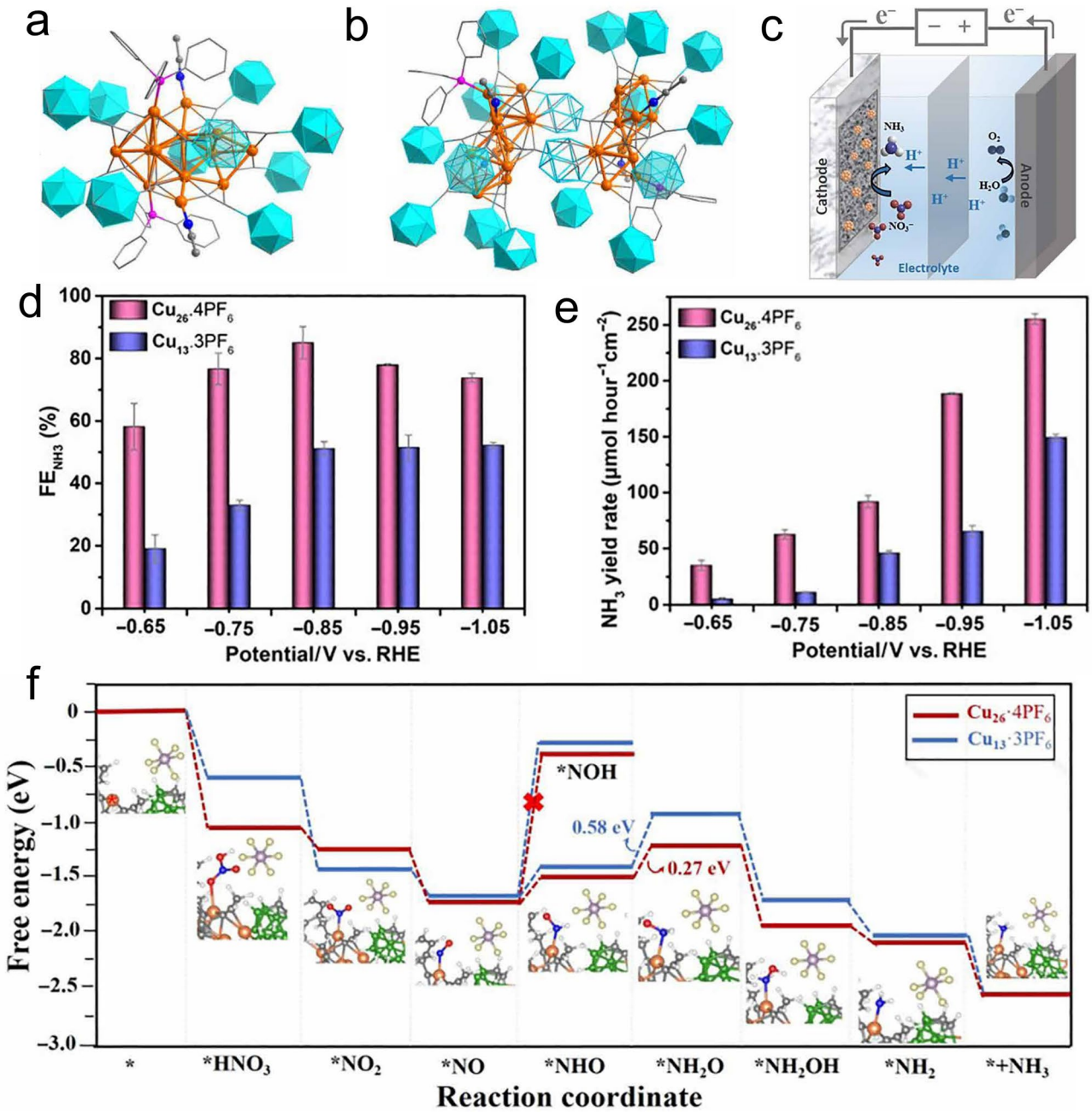

Fig. 6 Structure of **a** $Cu_{13}{\cdot}3PF_6$ and **b** $Cu_{26}{\cdot}4PF_6$·**c** Schematic illustration of NO_3RR. **d** Comparison of FE_{NH3} at various potentials. **e** Potential dependent NH_3 yield rate for $Cu_{13}{\cdot}3PF_6$ and $Cu_{26}{\cdot}4PF_6$. **f** Corresponding adsorption configurations of the reaction intermediates and Gibbs free energy in eNO_3RR. Cu, orange; F, yellow; P, violet; B, green; C, gray; O, red; N, blue; H, white. Reproduced with permission with Ref [53]. Copyright 2024 American Association for the Advancement of Science

CO_2 into useful chemical raw materials [142, 143]. Compared with other methods, the photocatalytic reduction approach has some unique merits. On one hand, photocatalytic method directly uses solar energy for CO_2 reduction and transformation, which is safe and pollution-free. On the other hand, the device for photocatalytic reduction is quite simple, and it can operate at very mild conditions, so the whole process is economically feasible [144–147].

Among a variety of photocatalysts, the artificial photosynthesis system using inexhaustible solar energy to

simultaneously reduce CO_2 and oxidize H_2O to produce valuable chemicals has been attracting more and more research attention [148, 149]. The current widely reported photocatalytic system usually comprises noble-metal-containing photosensitizers and/or organic dyes as electron donors, which are sophisticated and synthetically challenging to be available [150]. Therefore, it is highly desired to prepare a single component photocatalyst with suitable optical band and catalytic active center, that is similar to natural photocatalytic system, which can directly convert CO_2 and H_2O into value-added chemicals.

Metal nanoclusters, an emerging type of organic–inorganic hybrid material, composed of an organic layer and metal core, are promising candidates as a single component catalyst to realize the above goal [151, 152]. The ultrasmall size, well-defined configuration, and most importantly, the atomically precise structure can provide a perfect platform to probe the atomical level structure–performance understanding regarding the photocatalysis mechanism [153, 154].

Recently, the Zang group reported a stable Cu–S–N cluster photocatalyst with local protonated N–H groups, and such cluster can achieve ~ 100% selectivity for CO evolution under visible light. Specifically, two clusters of Cu_6-NH and Cu_6-N were prepared [54]. As shown in Fig. 7a, b, Cu_6-NH cluster possesses a distorted Cu octahedron, and one Cu atom coordinates with one N atom and two S atoms from three ligands. Such configuration is quite identical with the previously reported Cu_6-N cluster (Fig. 7c, d), except that the ligands in Cu_6-N are fully deprotonated, despite the two clusters having the same metal kernel (Fig. 7e). Both clusters have considerable absorbance capacities in the wavelength region of 400–550 nm, and comparable band gap energies (2.36 and 2.39 eV for Cu_6-N and Cu_6-NH, respectively). However, their visible-light-driven photoreduction capability of CO_2 showed some significant difference. Both clusters exhibited exceptionally high selectivity of CO with over 99%, but the CO evolution rate is much higher for Cu_6-NH than that of Cu_6-N (Fig. 7f). Furthermore, the Cu_6-NH photocatalyst demonstrated superior catalytic stability, as no detectable change is observed in the XRD patterns before and after the photocatalytic test (Fig. 7g). Finally, they conducted DFT calculations to elucidate the underlying physical origin, and found that, in the rate-determining step of forming *COOH, the Cu_6-NH cluster has a much lower energy barrier. This is due to the structural difference, that is, the presence of deprotonated pyrimidine N in Cu_6-N and protonated pyrimidine N in Cu_6-NH (Fig. 7h). The protonated pyrimidine N atoms in Cu_6-NH acted as a proton relay station to provide a local proton, hence facilitating the proton coupling process, leading to enhanced photocatalytic efficiency [54]. This study highlights the great promise of using Cu nanoclusters as photosensitive semiconductors for photoreduction of CO_2.

The precise structure of Cu nanoclusters allows the in-depth study of structure–property relationships in photocatalysis at the atomical level. Moreover, isomeric Cu nanoclusters can make the comparative structure–property relationship study feasible, as they have minimal structural difference. Isomeric Cu nanoclusters usually originate from the chiral isomerism, the structural isomerism, but the quasi-structural isomerism has been ignored for a long time. The quasi-structural isomeric Cu nanocluster usually displays comparative structural features, e.g., core geometric configuration, surface spatial arrangement.

In 2022, the Sun group reported two quasi-structurally isomeric Cu_{13} nanoclusters with highly similar kernel and different spatial arrangements of peripheral ligands (Fig. 8a) [49]. Both Cu13a and Cu13b clusters have a highly similar Cu_{13} kernel but different degrees of distortion (Fig. 8b, c). The formation of these two Cu cluster isomers is governed by the exotic chlorine ion, and also due to the charge transfer from Cl^- to Cu core, Cu13a presented lower superoxide radical ($O_2^{\bullet-}$) yield and higher singlet oxygen ($^1O_2$) compared to that of Cu13b. The conduction band minimum (CBM) is −1.20 and −1.26 V for Cu13a and Cu13b, respectively, so through the band gap value, the valence band maximum (VBM) is calculated as 0.74 and 0.66 V for Cu13a and Cu13b, respectively (Fig. 8d). More negative CBM value drives Cu13b more energetically feasible for $O_2^{\bullet-}$, while for Cu13a, the larger band gap favors the exchange of an electron with $^3O_2$, also more efficient for $^1O_2$ generation (Fig. 8e). Consequently, the two clusters demonstrated different performance particularly in selectivity in sulfides oxidation into sulfoxides. As summarized in Fig. 8f, despite methyl sulfide can be transformed into dimethyl sulfoxide by two clusters with nearly identical high conversion rates (near unity), Cu13a showed a certainly higher degree of enhancement than that of Cu13b [49]. This work provides a new pathway for boosting the photocatalytic selectivity of Cu nanoclusters.

https://doi.org/10.1007/s40820-024-01555-6

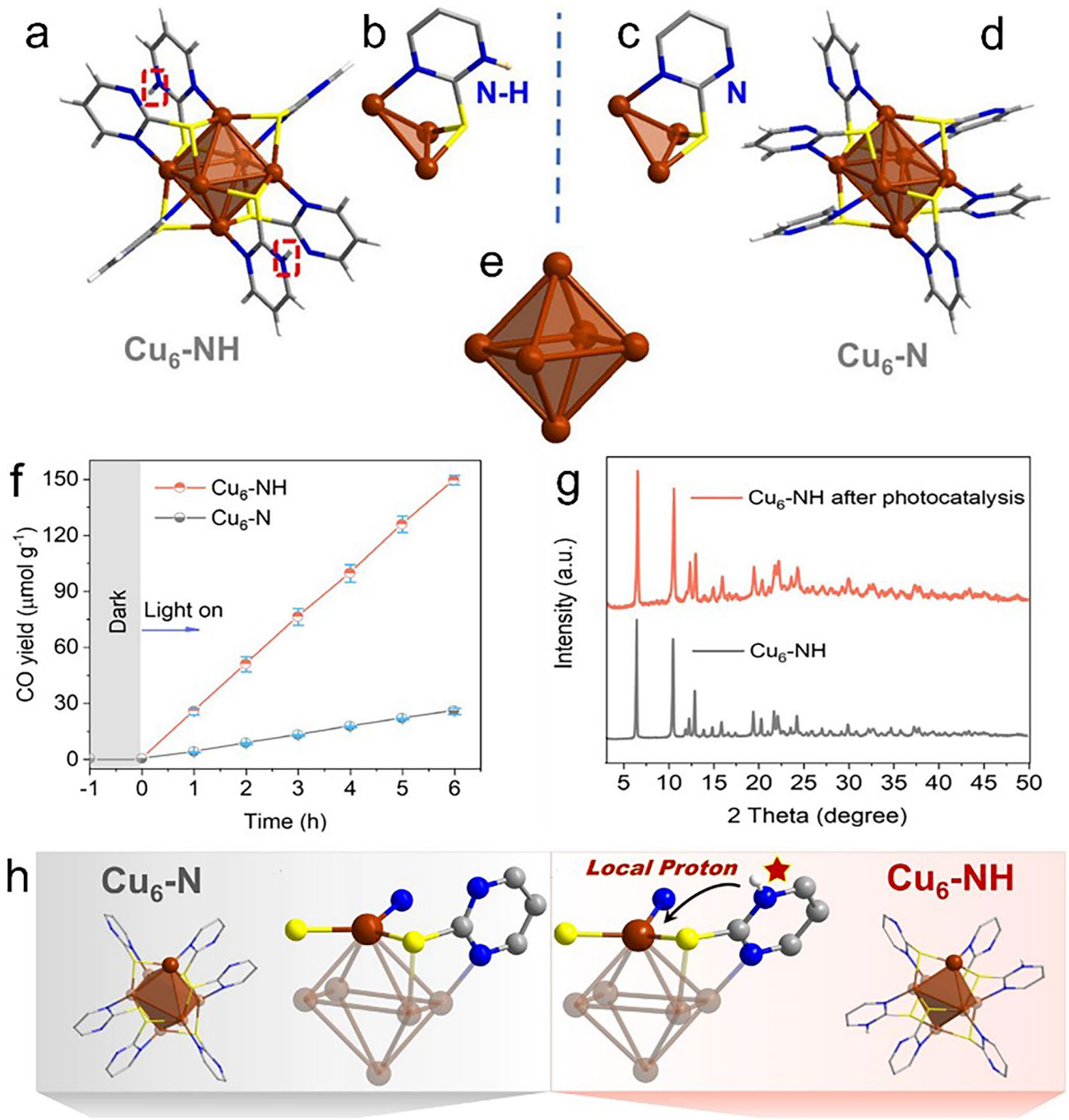

Fig. 7 Overall structures of the **a** Cu_6-NH and **d** Cu_6-N clusters. Coordination modes in **b** Cu_6–NH and **c** Cu_6–N. **e** Cu_6 framework; The molecule packing diagrams of **f** CO_2–CO photoreduction performances of Cu_6–NH and Cu_6–N. **g** PXRD patterns of Cu_6–NH before and after 24 h photocatalytic reaction. **h** Different angles showing the Cu_6 NC structures and the coordination environment around the Cu sites for Cu_6-N and Cu_6-NH. Color codes: brown, Cu; yellow, S; gray, C; white, H; blue, N. Reproduced with permission from Ref. [54], Copyright 2023 Wiley–VCH

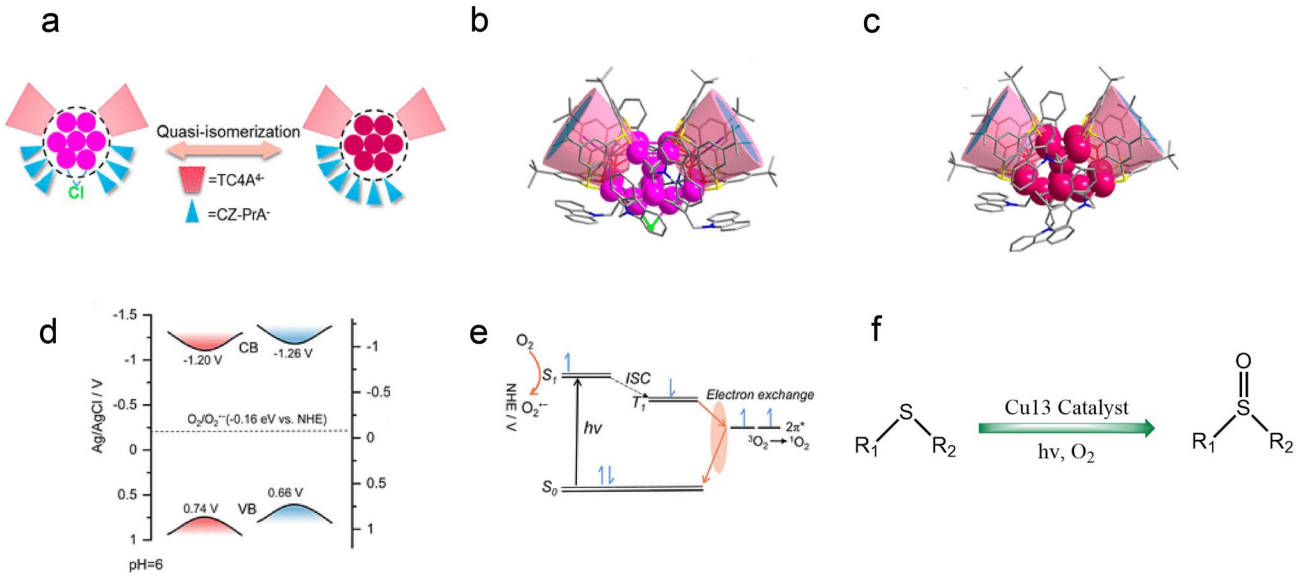

Fig. 8 **a** Schematic demonstration of the quasi-isomerization. **b, c** Side views of the molecular structures of Cu13a and Cu13b. **d** Schematic diagram for the band structures of Cu13a and Cu13b. **e** Mechanism of Cu13 cluster and $^3O_2$ for $^1O_2$ and $O_2^{\bullet-}$ photogeneration. **f** Oxidation of sulfides catalyzed by Cu_{13} nanoclusters. Color labels: red and purple, Cu; cyan, Na; gray, C; red, O; yellow, S; blue, N; green, Cl. Reproduced with permission from Ref. [49], Copyright 2022 American Chemical Society

In modern synthesis, bond-forming reactions are critical for generating new products, particularly, bond-forming reactions at mild conditions can find versatile applications in fine chemical synthesis, new drug discovery, and sustainable production of the industrial precursor. To that end, visible light photocatalysis is more advantageous as compared to thermal catalysis, however, developing high-efficiency, stable catalyst is the key [155]. Cu-based photocatalysis has shown great promise as an inexpensive and attractive method, compared to the expensive metal-complex and less stable organic dyes [156, 157]. Nevertheless, the cross-coupling reactions of aryl bromides and iodides are relatively easy to realize, but the cross-coupling reactions of aryl chloride remained extremely challenging.

In 2022, the Bakr and Rueping team reported a $[Cu_{61}(S^tBu)_{26}S_6Cl_6H_{14}]$ nanocluster (Cu_{61}NC)-based catalyst that can enable C-N bond-forming reaction of aryl chlorides under visible-light irradiation at ambient conditions [55]. As shown in Fig. 9a, the pronounced molecular ion is observed, and the experimental pattern agrees well with the simulated pattern. Figure 9b illustrates that it has two characteristic bands, and the crystal structure can be found inset. In the presence of base, at room temperature, the Cu_{61} NC cluster can catalyze the Ullman reaction for het(aryl) very well (Fig. 9c). The authors also proposed a plausible mechanism (Fig. 9d). Specifically, Cu NC reacts with the base forming CuNC-amine complex A first, then blue LED irradiation leads to the formation of complex B. After a SET process to give an electron to aryl chloride, the oxidized CuNC-Nu complex, a halide anion, and an arene radical were generated, evidenced by the fluorescence and quenching lifetime tests. After that, the radical attacks the CuNC-Nu complex, delivering the C–N bond formation and recovering the Cu_{61} clusters [55]. This study introduces atomically precise Cu clusters as a new family of photocatalysts for bond-forming reactions under mild conditions.

3.3 Cu NCs for Organic Reactions

3.3.1 Click Reaction

The perfect monodisperse and atomically precise nature of molecular metal nanoclusters can facilitate the development of detailed structure–activity relationships [158–160]. Using these atomically precise metal nanoclusters as catalysts can uncover new insights, but some of them may not be suited for this purpose. Specifically, a vast majority of these metal nanoclusters are protected by a shell of thiolate ligands [1,

 https://doi.org/10.1007/s40820-024-01555-6

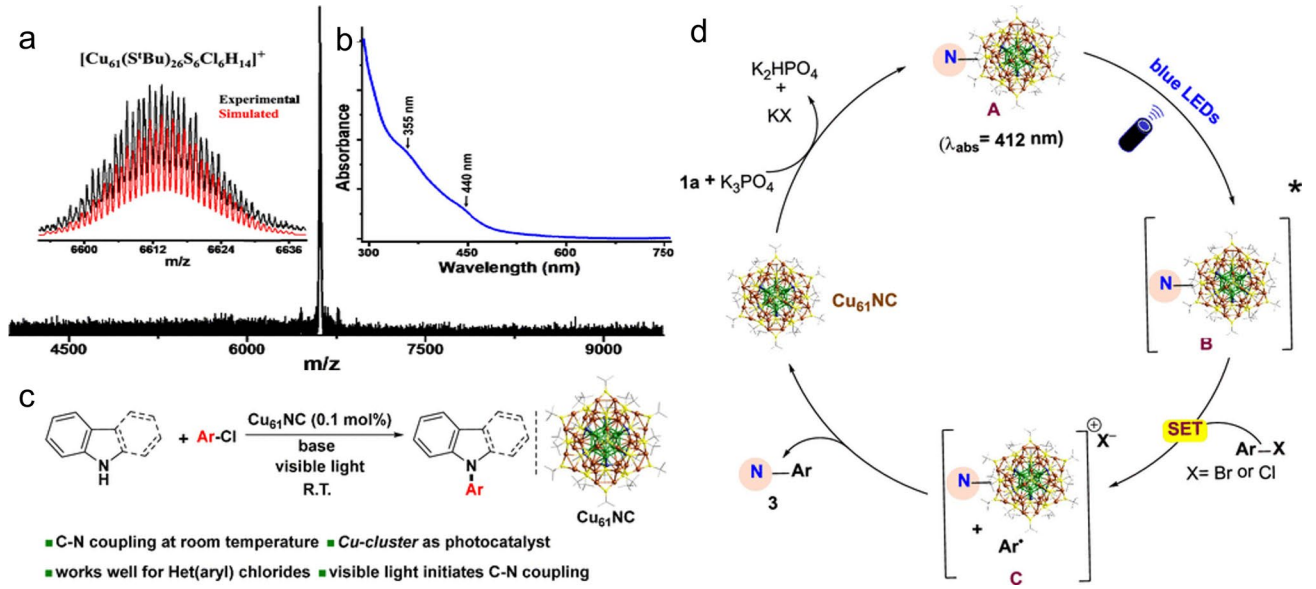

Fig. 9 ESI MS spectrum of Cu_{61} NC. The molecular ion peak is at m/z of 6613.5. Insets: **a** Comparison of experimental and simulated isotopic patterns. **b** UV–Vis absorbance spectrum showing two bands at 355 and 440 nm. **c** Cu_{61} NC catalyzed Ullmann C–N Coupling. **d** Proposed reaction mechanism. Reproduced with permission from Ref. [55], Copyright 2022 American Chemical Society

152]. These ligands can impart the clusters significant thermal and chemical stability, but they can also block some active sites and hence must be partially removed before catalysis can occur [161]. Meanwhile, the strong bonding strength of the metal-sulfur bond makes it hard to remove completely [161]. However, the harsh reaction conditions often lead to the significant structure or nuclearity change of the metal nanoclusters, making the structure–activity relationship unreliable. To address this issue, the researchers switched to other ligands, which do not require harsh pretreatment for activation. To that end, alkynyl molecules, phosphine ligand, halogen, hydride, and their mixed combination have been widely utilized to prepare atomically precise metal nanoclusters including Cu nanoclusters [56, 72, 73, 162].

In 2018, the Hayton group reported the synthesis of $[Cu_{20}(C{\equiv}CPh)_{12}(OAc)_6]$ cluster and its catalytic application in Click reaction [36]. Figure 10a shows the crystal structure of the Cu_{20} cluster, which has 4 THF molecules incorporated into the crystal lattice as solvates. It has a tetrahedral $[Cu_4]^{2+}$ core (Fig. 10b), which is encapsulated by a $[Cu_{16}(C{\equiv}CPh)_{12}(OAc)_6]^{2-}$ shell (Fig. 10c). There are 12 acetylide ligands in the $[Cu_{16}(C{\equiv}CPh)_{12}(OAc)_6]^{2-}$ shell distributed by 4 $[cyclo\text{-}Cu(C{\equiv}CPh)]_3$ units, which are located at the vertices of a tetrahedron, meanwhile, there are six acetate ligands situated at the edges of the tetrahedron (Fig. 10c). Then the Cu_{20} cluster was immobilized on dry, partially dehydroxylated silica, and the supported cluster catalyst displayed excellent performance toward the Click reaction of cycloadditions between benzyl azide and terminal alkynes. As demonstrated in Fig. 10d, the catalyst is effective for various terminal alkynes without harsh pre-treatment and even with a rather low cluster loading of 0.05 mol%. More importantly, X-ray absorption near edge structure (XANES) test after the catalytic test shows that the cluster undergoes no significant nuclearity changes under click reaction conditions [36]. It also indicates that the Cu species mainly kept as Cu(0) and Cu(I) in the cluster during the reaction process, where the Cu(I) species is well known to be the active site for click reaction. Great promises of using atomically precise Cu nanoclusters to examine the structure/activity relationship have been demonstrated in this study, especially for the non-thiolate protected Cu nanoclusters.

In nanocatalytic regime, elucidating single-atom effect of the nanocatalyst is interesting yet extremely challenging, as one single-atom modification can cause appreciable change to the overall particle's structure, not to mention that, the size polydispersity and ambiguous surface structure of the metal nanoparticle [163]. Nevertheless,

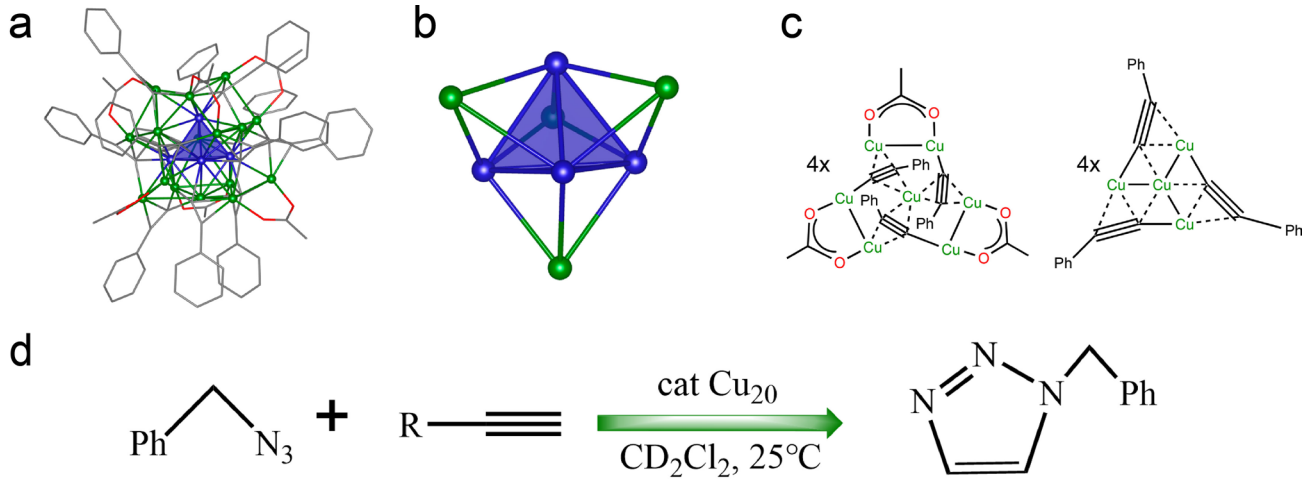

Fig. 10 **a** $[Cu_{20}(C{\equiv}CPh)_{12}(OAc)_6]{\cdot}C_4H_8O$. **b** Tetrahedral Cu_4^{2+} core (blue) and face-capping Cu atoms (green). **c** Ligand binding modes. **d** Cycloadditions catalyzed by Cu_{20} nanoclusters. Color legend: Cu = blue, green; C = gray; O = red. Reproduced with permission from Ref. [36], Copyright 2018 American Chemical Society

atomically precise metal nanoclusters have created great opportunities to tailor the chemical structure at the atomic level.

Recently, the Bakr and Rueping team reported the synthesis of $[Cu_{58}H_{20}PET_{36}(PPh_3)_4]^{2+}$ (Cu_{58}) and its analogue of $[Cu_{57}H_{20}PET_{36}(PPh_3)_4]^{+}$ (Cu_{57}) with one surface Cu atom removed, and Cu_{57} showed much higher catalytic activity toward [3 + 2] azide-alkyne cycloaddition (AAC, click reaction) than that of Cu_{58} [57]. As illustrated in Fig. 11a, Cu_{58} has a multishell architecture, and the metal skeleton possesses five concentric shells of $Cu_8@Cu_6@Cu_{24}@Cu_{12}@Cu_8$. Meanwhile, the ligand layer in Cu_{58} consists of a P_4 tetrahedron, an S_{12} icosahedron, and an S_{24} truncated cube. Cu_{57} has nearly the identical metal kernel structure except one Cu atom was removed on shell-4. Subsequently, the two nanoclusters were employed as catalyst for the click reaction. With the 0.025 mol% of Cu_{57} or Cu_{58} stoichiometric ratio, and in the presence of 1.5 h light irradiation, the product yields of 97% and 77% were achieved for Cu_{57} and Cu_{58}, respectively (Fig. 11b). In addition, both clusters showed good catalytic stability, as no obvious product yield decline was observed after three catalytic cycles (Fig. 11c). Overall, Cu_{57} performed more efficiently than Cu_{58} in the click reaction, and one single atom removal made great difference in the nanoclusters' catalytic activity [57]. This work may open a new avenue for the nanoparticles' catalytic design by targeted isostructural single-atom manipulation.

3.3.2 C–C Coupling Reaction

The C–C bond formation is a widely employed transformation in natural product synthesis, pharmaceutical synthesis, medicinal chemistry, and preparation of functional materials. So far, various catalytic methods have been developed for this important cross-coupling reaction. Among that, Sonogashira cross-coupling reaction is one of the most important and widespread used sp^2–sp^2 carbon–carbon bond formation reactions in organic synthesis, which is usually catalyzed by Pd and other transition metals [157, 164]. It can realize the coupling of aryl or vinyl halides with terminal acetylenes, but most of the catalysts suffer from that the undesired alkyne homocoupling side reaction is extremely difficult to suppress.

In 2023, the Rueping and Bakr group reported the $[Cu_{28}H_{10}(C_7H_7S)_{18}(TPP)_3]$ cluster (Cu_{28}; C_7H_7S: o-thiocresol; TPP: triphenylphosphine) with a defined defect for Sonogashira C–C coupling reaction. The skeleton structure of Cu_{28} is shown in Fig. 12a, and it features a centered Cu_{13} anti-cuboctahedron core, like the Cu_{25}, Ag_{19}, and Ag_{25} nanoclusters, and Cu_{28} also has a unique cage-like $Cu_{15}S_{18}P_3$ shell. Interestingly, Cu_{28} is a defective nanocluster which contains a surface vacancy, as one Cu atom is missing in one tetrahedron's vertex, and this vertex is expected to connect with a phosphine ligand. Subsequently, Cu_{28} was examined as a catalyst for Sonogashira C–C coupling reaction. Upon UV-LEDs irradiation, the desired C–C coupling

 https://doi.org/10.1007/s40820-024-01555-6

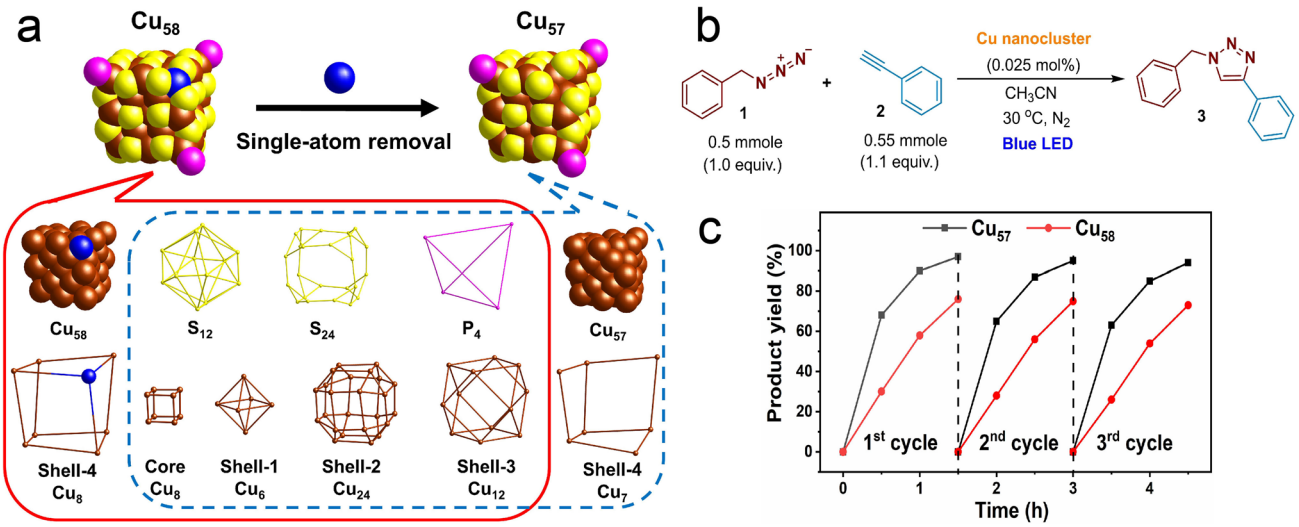

Fig. 11 **a** Crystal structure and dissection of Cu_{58} and Cu_{57}. **b** Cycloaddition between phenylacetylene and benzyl azide using Cu_{58} and Cu_{57} as catalyst under visible light. **c** Time-dependent product yields of Cu_{58}-catalyzed AAC under visible light. Brown and blue: Cu; yellow: S; pink: P. Reproduced with permission from Ref. [57], Copyright 2023 Wiley VCH

product with a high yield of 82% was acquired without the byproduct of homocoupling reaction (Fig. 12b) [58]. The authors then conducted the mechanistic control studies and proposed the tentative reaction mechanism (Fig. 12c). Upon blue-light irradiation, Cu_{28} was photoexcited (**A**), and it can induce a single electron transfer (SET) process with aryl iodides to yield the Ar-radical (**C**) and oxidized Cu_{28}^{+} (**B**). The Ar-radical then attacks the alkyne C–C triple bond to generate vinylic type C-radical intermediate (**D**). Another single electron transfer process to B can regenerate the Cu_{28} photocatalyst. Note that the C–C triple bond can be activated by Cu_{28} through forming a Cu NC-π-alkynyl type complex hence easily being attacked by the Ar-radical. The authors detected a little stilbene-type byproduct in GC–MS measurement generated by a hydrogen atom transfer (HAT) process. Finally, the base-induced deprotonation of vinyl cation E leads to the desired Sonogashira C–C coupled product [58]. Upon the photoexcitation of blue-LEDs, the oxidation state of the Cu_{28} cluster undergoes a transient transition from 0 to I, form $[Cu_{28}]^{+}$ NC, while after the second single electron transfer (SET) process, it returns to the ground state of Cu_{28}. The results demonstrate that Cu_{28} is an active photocatalyst enables the SET process with aryl iodides to produce Ar-radical which attacks the C–C triple bond, totally preventing the formation of homocoupling product. This investigation paves a way to acquire Cu NCs with defined surface defects as active sites, and more importantly, these defective Cu NCs can serve as model systems to provide profound understanding on defect effect for heterogeneous catalysis.

Recently, Biswas et al. reported a hydride-free $[Cu_7(SC_5H_9)_7(PPh_3)_3]$ (Cu_7) nanocluster (NC), which demonstrated remarkable specificity in a photoinduced C–C coupling reaction [59]. The Cu_7 NC has a metal core with 4 Cu atoms forming a tetrahedron (Fig. 13a), and three Cu atoms are connected with the bottom face of the tetrahedron with another three Cu atoms (Fig. 13b). The metal–ligand binding configurations are shown in Fig. 13c, d, where the thiolate ligands mainly adopt the bridging modes, and three P atoms connected with three Cu atoms directly. Interestingly, the Cu_7 NC exhibits intriguing photoluminescence (PL). Upon exciting the cluster at 395 nm, a robust PL emission is observed at room temperature with an emission peak occurring at 436 nm. Such outstanding photophysical properties inspired the authors to explore the Cu_7 NC as catalyst for photoinduced C–C bond formation reaction. Under purple light irradiation from LEDs, the Cu_7 NC (5 mol% Cu) was able to catalyze the C_{sp2}-C_{sp} coupling reaction between phenyl iodide and phenyl acetylene to generate the desired product with high yield (Fig. 13e). With the aid of control experiments and DFT calculations, the authors also proposed tentative reaction mechanism (Fig. 13f). Initially, the Cu active site in Cu_7 NC binds to alkyne to form an intermediate of **Int-I** in the presence of MeONa. Subsequently, **Int-I** is photoexcited to generate **Int-I***, which engages the

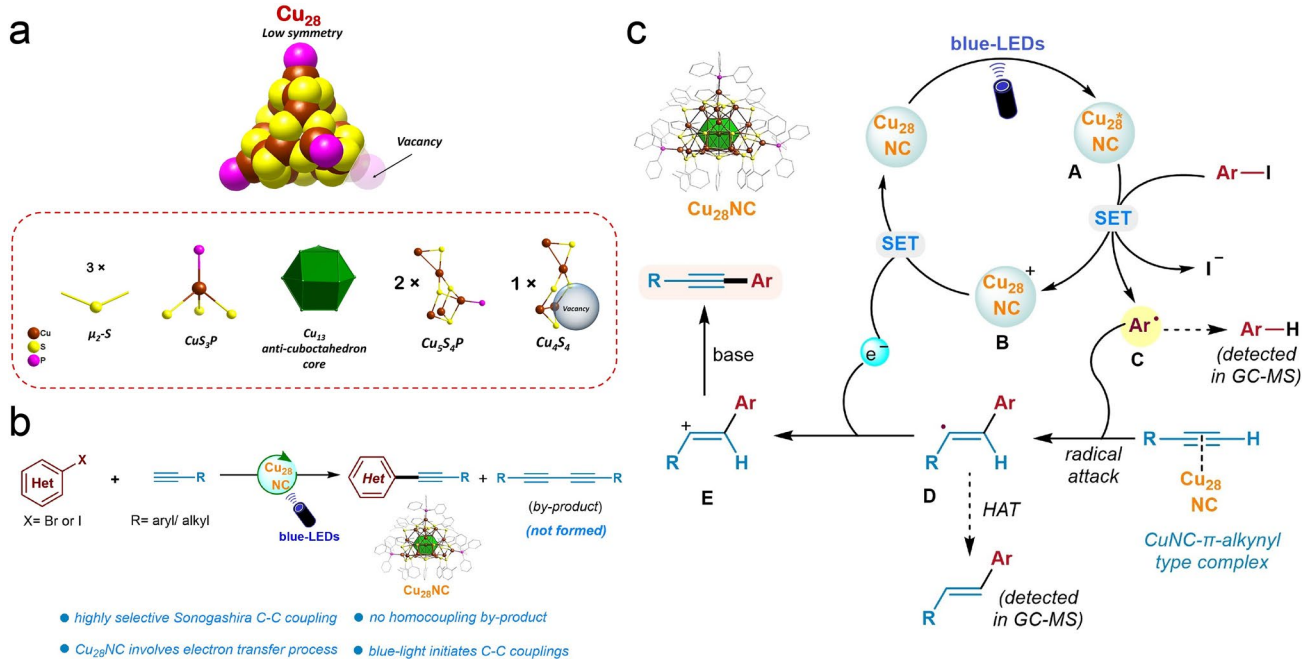

Fig. 12 **a** Structure of Cu_{28} nanocluster. **b** Sonogashira C–C coupling reaction. **c** Proposed reaction mechanism. Reproduced with permission from Ref. [58], Copyright 2023 Wiley VCH

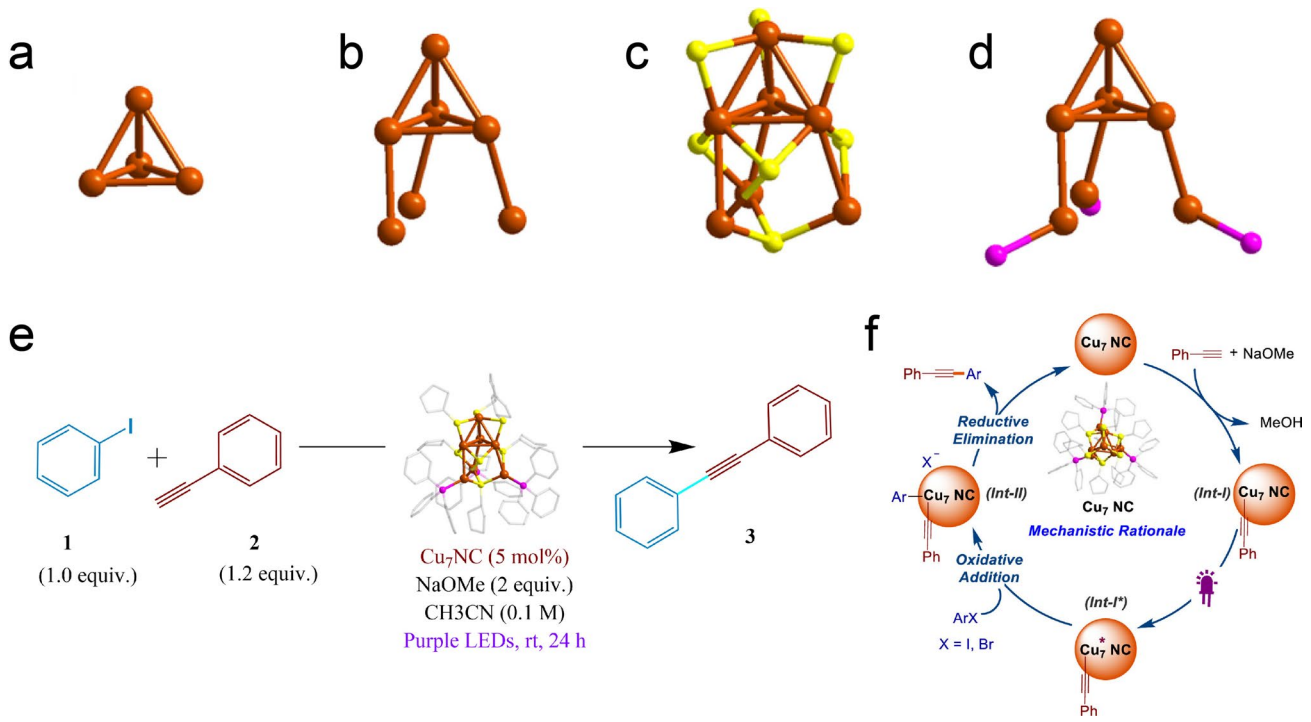

Fig. 13 **a** Cu_4 head. **b** Three Cu atoms connected with the Cu_4 head. **c** S-Cu binding configuration and **d** P-Cu binding configuration in the Cu_7 core. **e** Reaction optimization of C_{sp2}–C_{sp} cross-coupling in the presence of Cu_7 NC and **f** proposed reaction mechanism. Cu, brown; S, yellow; and P, magenta. Reproduced with permission [59], Copyright 2024 American Chemical Society

 https://doi.org/10.1007/s40820-024-01555-6

oxidative addition step to yield the intermediate of **Int-II**. The following reductive elimination of **Int-II** produces the final product, along with the release of the Cu_7 NC. In this mechanistic rationale cycle, the oxidative addition step is identified as the rate-determining step [59]. This work provides some mechanistic insights of using atomically precise Cu nanoclusters for C–C coupling reactions, and underscore the great potential of hydride-free Cu nanoclusters for catalysis.

3.3.3 A^3 Coupling Reaction

To forge new C–C and C–N bonds, three-component dehydrogenative coupling reaction represents a new practical methodology. Yet, to realize all-in-one three-component dehydrogenative coupling in a single catalytic system remains very challenging [165]. For instance, to fulfill the efficient synthesis of propargylamines including C1-propargylamines, Cu compounds are the most widely recognized catalysts to implement the A^3 coupling reactions or redox-A^3 coupling reactions, but the reaction conditions are rather harsh [166]. Therefore, a Cu-based catalytic system with high efficiency and regio-selectivity with broad substrate scope working under mild conditions is highly desirable.

Recently, the Zang group reported a tridentate N-heterocyclic carbene ligand stabilized $[Cu_3(NHC)_3(PF_6)_3]$ (Cu_3NC) cluster for both A^3 coupling reactions and redox-A^3 coupling reactions [60]. The crystal structure of the NHC ligand and Cu_3NC are shown in Fig. 14a, b, respectively, where the NHC ligand endows the Cu_3NC with dual attributes of flexibility and rigidity. On one hand, the stable Cu–C and Cu–N bonds between the NHC ligand shell and the metal core favors the stability of the Cu_3NC. On the other hand, the pyridine of the N-heterocyclic carbene has somewhat dynamic balance between the aliphatic amines and the pyridine to protect the catalytic centers and prevent the Cu_3NC deactivation. Such dynamic balance endows Cu_3NC with flexible features. Consequently, high activity and high regioselectivity can be achieved in all-in-one A^3 coupling reactions with inert substrates at room temperature (Fig. 14c), as manifested by 71 examples of A^3 coupling reactions and 14 examples of redox A^3 coupling reaction, both up to 99% yield [60]. The following mechanistic and control experimental tests demonstrated that the remarkable catalytic performance originates from the flexible and rigid dual attributes of the Cu_3NC.

It is worth noting that most ligand protected Cu nanoclusters feature a core–shell framework hence the active sites can be blocked by metal–ligand shell or surface passivation units. Therefore, a strategy that can largely expose the metal active sites is long pursued for catalytic coupling reaction. In 2023, Xu et al. reported a novel approach to construct array-based $([Cu_8(Tf\text{-}dpf)_4(NO_3)_2](NO_3)_2$ clusters [61]. Compared with the $([Cu_8(RS)_6(PPh_3)_4(MeCN)_4H]^+$ with the cubic core, the above array based Cu_8 cluster displays largely uncoordinated metal sites, hence exhibited significantly enhanced catalytic activity in the "aldehyde-acetylene-amine" A^3-coupling reaction for synthesizing propargylamines. It shows the great potential to fabricate array-based Cu nanoclusters for A^3 coupling reaction and beyond [61].

3.3.4 Synthesis for Indolizines

To realize the practical catalytic application of Cu nanoclusters, the long-term stability remains a long-standing challenge. In the regime of coinage metal nanocluster, compared with Au, Ag, and Au/Ag alloy clusters, the study of Cu nanoclusters lags far behind, mainly due to the high reactivity of Cu and low standard reduction potential ($E^0_{Cu2+/Cu+} = 0.34$ V, $E^0_{Cu+/Cu} = 0.52$ V) [22]. The surface organic ligand such as thiolate molecules, alkynes, halides, hydride can improve the stability due to the formation of strong chemical bonds, but the long-term stability for some specific organic reactions are still unsatisfactory. These ligands are considered as soft base, and Cu^{2+} or Cu^+ ions belong to soft acid; therefore, the ligand–metal interaction fits the Pearson's hard/soft acid/base theory [167].

In a recent study conducted by the Li and Ni team, pyrazolate (denote as Pz) ligands were employed to synthesize Cu_8 nanoclusters [62]. Pz is a soft base, and thanks to the high pK_a value of 19.8 for deprotonated pyrazole [168], Pz protected Cu clusters are expected to exhibit exceptional alkali-resistant capability. As determined from SCXRD (Fig. 15a), the flexible bis-pyrazole ligands (H2L1) can transform into two novel deprotonated bis-pyrazole ligands (L2 and L3), and all these L2 and L3 ligands can assemble

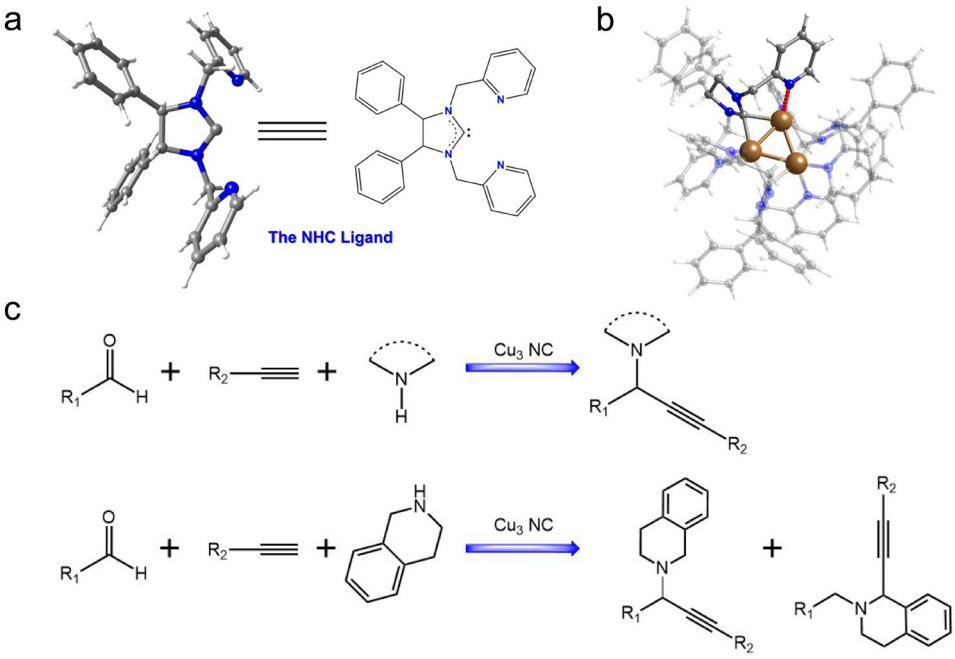

Fig. 14 **a** Structure of the N-heterocyclic carbene (NHC) ligand. **b** Total structure of the Cu_3NC. **c** Cu_3NC catalyzed both the A^3 coupling reaction and the redox-A^3 coupling reaction. R_1, R_2, R_3 and R represent kinds of functional group. Reproduced with permission from Ref. [160], Copyright 2023 Nature Publishing Group

with Cu^+ to yield Cu_8 nanoclusters. The crystal of Cu_8 clusters can keep intact in various organic solvents, highly concentrated acid, saturated alkali, oxidant, and boiling water, and still are fine for SCXRD test. More impressively, the introduction of organic acid or base (100 eq. HOAc, or 400 eq. dibutylamine) cannot impose structural decomposition, neither, confirming the remarkable stability never documented for Cu nanoclusters (Fig. 15b). Subsequently, the synthesis for indolizines from 2-pyridinecarboxaldehyde derivatives, terminal alkynes and secondary amines was tested using Cu_8 nanocluster as a catalyst. Interestingly, the reaction cannot proceed without Cu_8 cluster as the catalyst (Fig. 15c). The optimized condition is 0.005% mol of substrates. Other Cu nanoclusters such as Cu_{10} or Cu_{18} had a much lower yield, as they are not stable in basic conditions (Fig. 15d). Consequently, the turnover frequency (TOF) of Cu_8 nanoclusters can reach 3880 h^{-1}, about 3 orders of magnitude larger than the reported catalysts toward the synthesis of indolizines [62]. This study provides a new strategy to synthesize pyrazolate-protected Cu nanoclusters with ultrahigh chemical stability for practical applications.

3.3.5 Reduction of Ferricyanide to Ferrocyanide

Ferricyanide ($[Fe(CN)_6]^{3-}$) is an environmentally unfriendly material that readily reacts with acids to produce toxic hydrogen cyanide gas. The catalytic reduction of $[Fe(CN)_6]^{3-}$ to ferrocyanide ($[Fe(CN)_6]^{4-}$) is one effective strategy to limit the toxicity of $[Fe(CN)_6]^{3-}$ [169].

In a recent study, the Luo and Sun team reported the $Cu_{18}H(PET)_{14}(PPh_3)_6$(isothiocyanate)$_3$ ($Cu_{18}H$ in short) nanocluster [63], which exhibits excellent catalytic performance in the reduction of ferricyanide. $Cu_{18}H$ comprises a pseudo D3-symmetrical triple-stranded helical Cu_{15} kernel, and can be structurally described as layer-by-layer combination of multiple chiral Cu nanoclusters linked through copper-thiolate bonds. Remarkably, the aggregate state of the $Cu_{18}H$ nanoclusters can catalyze electron transfer reactions efficiently. To assess its catalytic capability, ultraviolet/visible absorption spectroscopy was used to monitor the reduction process. When $Cu_{18}H$ and $NaBH_4$ were added simultaneously, $[Fe(CN)_6]^{3-}$ can be completely converted into $[Fe(CN)_6]^{4-}$ very rapidly, and the solution turned into colorless within 14 s. In a control test, the reduction reaction of $[Fe(CN)_6]^{3-}$ without $Cu_{18}H$ required

 https://doi.org/10.1007/s40820-024-01555-6

16 min. It indicates that $Cu_{18}H$ has good catalytic reactivity for the reduction of $[Fe(CN)_6]^{3-}$ [63]. This study makes an interesting model for investigating and elucidating the aggregated state of copper nanoclusters.

3.3.6 Hydrogenation of Cyclohexanone

The chemical hydrogenation of cyclohexanone is among the most important and prevalent transformations in industrial organic synthesis, thanks to its effectiveness and economic viability [170, 171]. A previous report suggested that copper hydride nanoclusters are very promising for catalyzing the hydrogenation of carbonyl compounds, despite that there are challenges to control the product selectivity [172].

In a recent work done by Sun et al., a cluster of $[Cu_{66}Cl_8(PPh_3)_8(SC_2H_5)_{32}H_{24}](SbF_6)_2$ (Cu_{66} in short) was synthesized and its catalytic performance toward the hydrogenation of cyclohexanone was examined [64]. Cu_{66} contains an orderly of 16 Cu_4 squares, and the ligands coordinate to the surface of the cluster in a regiospecific manner, displaying square pattern as well. To enhance the monodispersity and stability of the cluster catalyst, the Cu_{66} nanoclusters were immobilized on carbon black (XC-72) to afford the Cu_{66}/XC-72 catalyst, and it demonstrated an unprecedented performance toward the hydrogenation of cyclohexanone. The selectivity of cyclohexanol is nearly 100%. Under specific conditions, complete conversion of cyclohexanone to the desired product was achieved within 40 h. The authors also tested all the other Cu catalysts, including $(Cu(CF_3CO_2)_2$, CuCl, $Cu_{54}Cl_{12}(NO_3)_{12}(SC_4H_9)_{20}S$ (Cu_{54}), $Cu_{50}(PhCOO)_{10}(4\text{-F-PhS})_{20}(PPh_3)H_2$ (Cu_{50}), $SeCu_{20}(PhSe)_{12}(PPh_3)_2(C_6H_5COO)_6$ (Cu_{20}), and $[Cu_{25}(SPhCl_2)_{18}H_{10}]^{3-}$ (Cu_{25}), but they showed significantly lower yields for the corresponding product. Moreover, the Cu_{66}/XC-72 catalyst exhibited no significant decay in cyclohexanol product selectivity, highlighting the robustness of the Cu_{66}/XC-72 catalyst [64]. This study showcases Cu nanoclusters have high stability and exceptional catalytic activity in the hydrogenation of carbonyl compounds, envisioning a bright future in both fundamental research and practical applications.

3.4 Cu NCs for Other Reactions

Atomically precise Cu nanoclusters can also find versatile catalytic applications toward other chemical reactions. One typical reaction is the catalytic hydrogenation of nitroarene. It is worth noting that the catalytic hydrogenation of toxic nitroaromatics into non-toxic amino molecules is a quite efficient and economical method, as amino molecules are valuable intermediates for pharmaceuticals and dyes [169, 173, 174]. Coinage metal nanoclusters have been emerging as a new type of important hydrogenation catalysts, and the catalytic hydrogenation of 4-nitrophenol into 4-aminophenol in the presence of BH_4^- reducing agent has been employed as a model reaction in several previous studies [32, 92, 95, 175].

In 2023, Luo et al. reported an intrinsically chiral Cu hydride-rich nanocluster of $[Cu_{57}H_{20}(PET)_{36}(TPP)_4]^+$ ($Cu_{57}H_{20}$) and its catalytic activity toward reduction of 4-nitrophenol [56]. Single crystal X-ray diffraction measurement shows that the unit cell of the $Cu_{57}H_{20}$ cluster contains a pair of enantiomers, C-$Cu_{57}H_{20}$ and A-$Cu_{57}H_{20}$ (C, clockwise; A, anti-clockwise) (Fig. 16a). The hydride positions were further validated by DFT optimization of the model cluster of $(Cu_{57}H_{20})_{opt}$. Interestingly, the DFT analysis also suggests that the interfacial μ_3-H in $(Cu_{57}H_{20})_{opt}$ can be transformed into an interstitial μ5-H species in the perfect cluster of $(Cu_{57}H_{20})_{opt}$ as long as the vacant position is recovered by the 58th Cu atom (Fig. 16b). The $Cu_{57}H_{20}$ cluster was then employed as the catalyst to catalyze the reduction of 4-nitrophenol. The reaction process was monitored by UV–vis absorption spectra (Fig. 16c), where strong absorbance peak at 400 nm from 4-nitrophenol decreased rapidly in 20 min and the absorbance peak at 300 nm from 4-aminophenol increased. The bright yellow solution also turned colorless. Using the absorbance change at 400 nm as metric, the reduction adopts a pseudo-first-order reaction kinetics, and the reaction rate was calculated as 18 min^{-1} (Fig. 16d). A control experiment in the absence of $Cu_{57}H_{20}$ was also conducted, and no reduction occurs on 4-nitrophenol when adding BH_4^-, probably due to the high activation barrier between the repelling 4-nitrophenol anion and BH_4^- [176]. Finally, the authors performed a 4-nitrophenol reduction test by using BD_4^- to check the accessibility of the hydride in $Cu_{57}H_{20}$. After the catalytic test, the cluster was examined by the ESI–MS measurement (Fig. 16e). It shows well defined peak feature of $[Cu_{57}H_{19}D(PET)_{36}(TPP)_4+Cu]^{2+}$, indicating one H^- is indeed replaced by one D^- of BD_4^-, that means, the exposed interfacial μ_3-H might be involved in the catalytic reaction [56]. By using defective $Cu_{57}H_{20}$ cluster as model catalyst, this work offers atom-precise insights into the vacant defect role in catalysis.

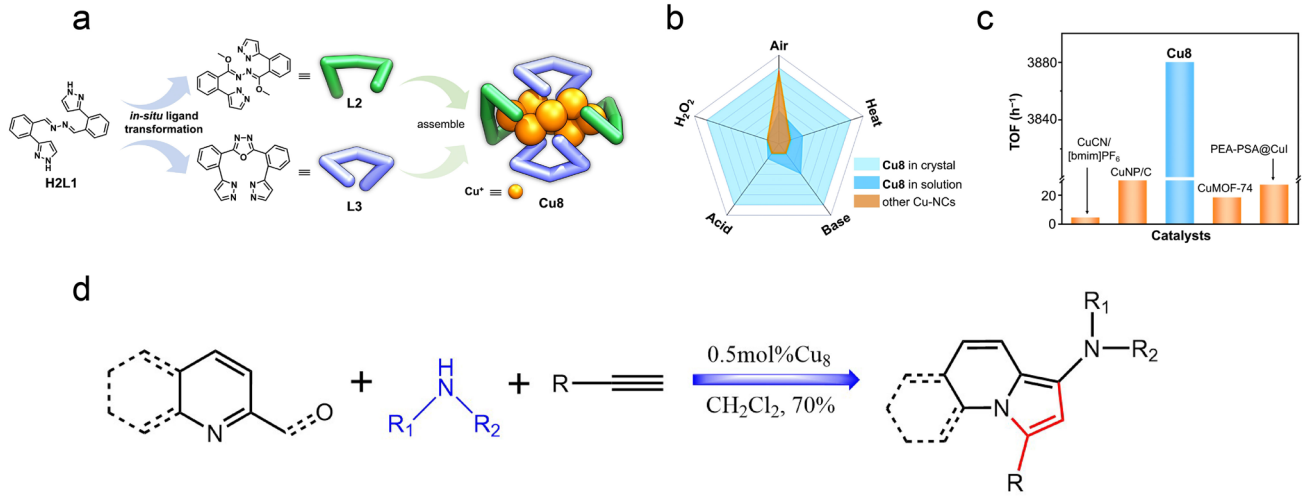

Fig. 15 **a** Schematic illustration for preparing pyrazolate-protected Cu_8 nanocluster. **b** Radar chart of various factors for the guidance and assessment of chemical stability of Cu_8 and other Cu-NCs. **c** TOF comparison for the indolizine synthesis based on Cu_8 and other catalysts. **d** Indolizines synthesis catalyzed by Cu_8 nanoclusters. Reproduced with permission from Ref. [62], Copyright 2023 Wiley VC

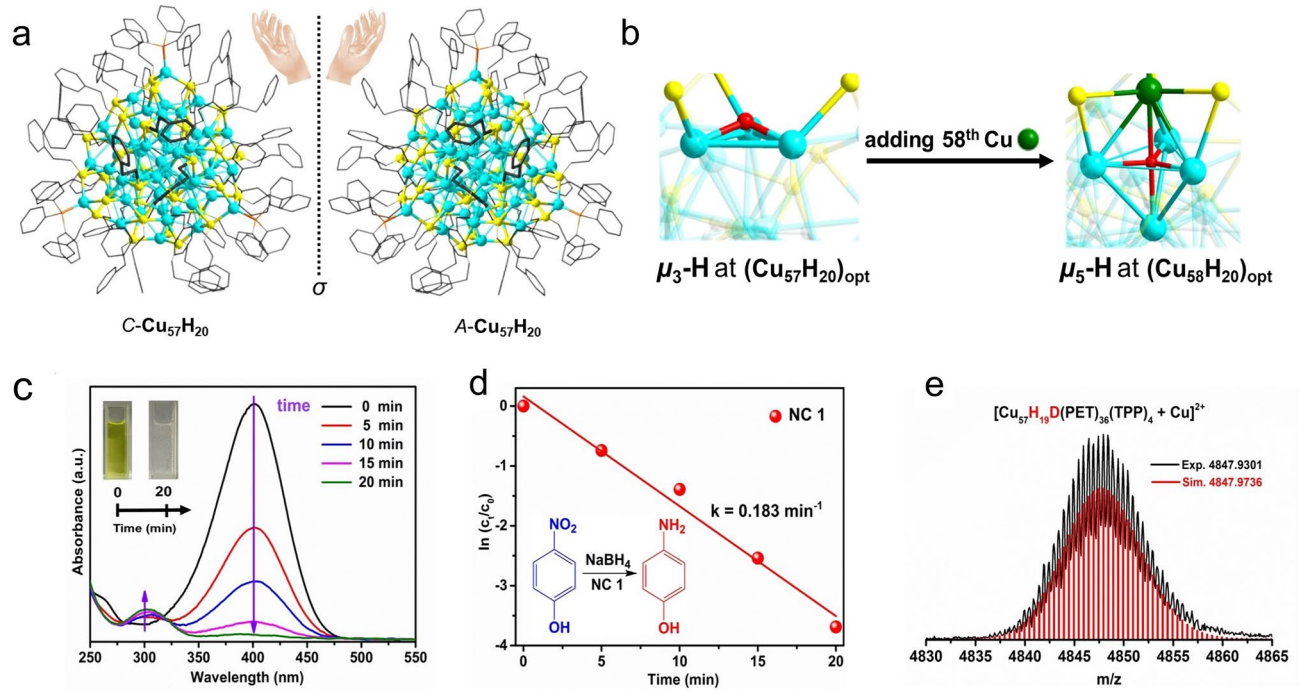

Fig. 16 **a** Total structures of the C–$Cu_{57}H_{20}$ and A-$Cu_{57}H_{20}$ isomers. **b** Transformation of a μ_3-H in $(Cu_{58}H_{20})_{opt}$ into a μ_5-H in $(Cu_{58}H_{20})$opt. **c** Absorption spectra versus time. **d** Plot of $\ln(C_t/C_0)$ versus time for 4-nitrophenol reduction. **e** ESI–MS spectrum after catalytic reaction with $NaBD_4$. Color labels: Cu, turquoise; C, gray; P, orange; S, yellow; red, H; yellow, S. Reproduced with permission from Ref. [56], Copyright 2023 Wiley–VCH

In addition, a very small change in composition can make a big difference in structure and catalytic performance for some specific catalytic reactions. In a recent report, the Wang and Jiang team disclosed the dramatic difference between $Cu_{20}H_8$ and $Cu_{20}H_9$ clusters in catalysis [65]. Specifically, two copper hydride clusters, $[Cu_{20}H_9(Tf\text{-}dpf)_{10}]\cdot BF_4$ ($Cu_{20}H_9$) and $[Cu_{20}H_8(Tf\text{-}dpf)_{10}]\cdot(BF_4)_2$ ($Cu_{20}H_8$) (Tf-dpf = N, N′-di(5-trifluoromethyl-2-pyridyl)formamidinate)

 https://doi.org/10.1007/s40820-024-01555-6

were fabricated, and both have twenty Cu atoms and ten amidinate ligands but with one hydride difference in the ligand shell. Such differences led to drastically different geometric and electronic structures, resulting in different catalytic properties. $Cu_{20}H_8$ showed 25 times higher catalytic activity than $Cu_{20}H_9$ in the conjugate reduction of cinnamaldehyde, mainly due to the easier dissociation process of a Tf-dpf$^-$ ligand in $Cu_{20}H_8$ [65]. This work highlights the sensitivity of structure and composition toward catalytic reactions by using atomically precise copper hydride nanoclusters as catalysts.

Recently, the Shen group found that the open metal site plays a critical role in the catalytic reduction of 4-nitrophenol by using two Cu_{41} nanoclusters as model catalysts [46]. Specifically, two isostructural Cu nanoclusters of $[Cu_{41}Cl_2(2\text{-}FC_6H_4S)_{12}(CF_3COO)_6(PPh_3)_6H_{19}]^{2-}$ (1H) and $[Cu_{41}(2,5\text{-di-Methyl-}C_6H_3S)_{12}(BO_3)_3Cl_3(PPh_3)_6H_{19}]$ (2H) were prepared and fully characterized, and the main structural difference of them lies in the absence or presence of two additional chlorides on the surface, which in turn heavily governs the exposure of metal sites. The 2H cluster with more open active sites exhibited ~ sixfold increase of rate constant in the catalytic reduction of 4-nitrophenol than 1H cluster [46]. This work manifests that atomically precise Cu nanoclusters can serve as catalyst models to directly visualize the active sites that drive the chemical transformation. Meanwhile, the same group also discovered that the small distinctions in two carboxylate-protected Cu_{20} clusters can cause distinct catalytic performance toward 4-nitrophenol reduction [66]. Two clusters $Se@Cu_{20}(PhSe)_{12}(PPh_3)_2(C_6H_5COO)_6$ (Cu_{20}-1) and $Se@Cu_{20}(PhSe)_{12}(PPh_3)_2(CF_3COO)_6$ (Cu_{20}-2) share with the identical metal skeleton and similar ligand distributions, and the main difference is the carboxylate ligand: $C_6H_5COO^-$ for Cu_{20}-1 while CF_3COO^- for Cu_{20}-2. Consequently, Cu_{20}-1 has a catalytic activity enhancement of 16-fold than Cu_{20}-2. Such catalytic performance distinction is attributed to the carboxylate effect, that is, the functional group (-$C_6H_5CO_2$ or -CF_3CO_2) altered the electronic structure of the Cu nanocluster [66].

4 Challenges and Perspectives

The last decade, especially the recent five years, have witnessed great success in atomically precise Cu nanoclusters, including synthesis, structural analysis, property exploration, and various catalytic applications. Despite the significant progress, there are still some important obstacles for nourishing the atomically precise Cu nanocluster field, especially in both synthetic regime and catalytic field. Some possible challenges and future perspectives are discussed below, aiming to motivate or advance this fast-growing field:

1. High-efficiency synthetic method to obtain atomically precise Cu nanoclusters is still highly desired. Compared with the fruitful achievements in Au and Ag nanoclusters, the synthesis and total structure determination of Cu nanoclusters have been lagging behind, probably due to the variability of Cu valence states. It is known that the subtle reaction conditions may affect the output of the final product, e.g., the solvent, the reaction temperature, the ligand (discuss below), the reducing agent, the pH value in the reaction system, the stoichiometric ratio of all the reactants, etc. For example, by using CH_2Cl_2 as the solvent, the Cl atoms can coordinate with Ag and become the capping ligand in alkynyl-protected Ag_{112} nanoclusters [177], and it might also be applicable for preparing Cu nanoclusters. More importantly, the current synthetic methods of atomically precise Cu nanoclusters are heavily dependent on the "the-trial-and-error" efforts, which are quite tedious, expensive, and low efficient. High throughput synthesis with the aid of artificial intelligence or machine learning technique represents an embryonic avenue yet still have a long way to go [178, 179].
2. The role of ligand should be carefully considered. The choosing of ligand molecule not only affects the synthesis, but also plays a critical role in the catalytic process. Thiolate, alkynyl molecule, hydride, halogen, phosphine, N-heterocyclic carbene, inorganic anions (e.g., BF_4^-, CH_3COO^-) are most widely employed ligand molecules for stabilizing Cu nanoclusters, but they possess different binding strength to the Cu core. It is commonly believed, the surface ligand can block some active sites for catalysis [161], as they can inhibit the reactants for accessing the metal sites. However, more and more cases have shown that, the ligand can facilitate the catalytic process, e.g., accelerate the transfer of the reactants or intermediates via weak interactions. Weak surface ligand is more easily stripped off or exchanged by the reactant to create catalytic sites [10]. Moreover, the type of ligand molecule affects the catalytic activity drastically, e.g., Tsukuda group reported that alkynyl-protected Au_{25} clusters exhibited markedly higher HER activity than thiolate-protected Au_{25} molecules [180], while our group discovered that, the

Faradaic efficiency of CO for alkynyl-protected Ag_{32} clusters is much higher than the thiolate and phosphine ligand co-protected Ag_{32} clusters in eCO_2RR [32]. Such catalytic property difference is attributed to the electronic structure change owing to the electronic perturbation of the π-conjugated units [72]. Even with the same type of molecule in ligand, the steric hindrance and electronic structure can affect the catalytic properties, e.g., using bulky ligand may create some low coordinated or undercoordinated metal sites for catalysis [159, 181]. The Xie group found that, in the oxygen evolution reaction catalyzed by three thiolates protected Au_{25} nanoclusters, *p*-mercaptobenzoic acid stabilized Au_{25} nanoclusters exhibited markedly superior catalytic performance, simply because the ligand's stronger electron-withdrawing ability can create more partial positive charges on Au(I) as active site for facilitating feasible adsorption of OH^- in alkaline media [182]. Yoo et al. found that the locally induced hydrophobicity by bulky alkyl functionality near the surface of the $Ag_{25}(SR)_{18}$ cluster dramatically enhanced the eCO_2RR activity, where the hydrophobic Ag_{25} cluster exhibited remarkable selectivity for CO (FE_{CO} > 90%) and achieved a high current density of up to -240 mA cm^{-2} with excellent durability lasting for over 120 h [183]. Nevertheless, the ligand role of atomically precise Cu nanoclusters during the synthetic process and catalytic duration remains largely to be explored.

3. The metal core tailoring. The metal core configuration and atomic spatial arrangement can be critical for exposing available catalytic active sites for Cu nanoclusters. So far, there are core-shell, rod-like, array-like core structure and other core configurations for Cu nanoclusters, but a trade-off between activity, selectivity and stability must be taken into account for specific catalytic reactions [69]. More profoundly, more dedicated core structure engineering might be necessary for Cu nanoclusters. Vacancy engineering has demonstrated great potential, which is expected to catch more future research attention [58]. Another important direction is alloying other metals to form atomically precise Cu–alloy nanoclusters. For catalytic reactions, the size, composition, configuration, electronic structure are the main factors that influence the catalytic performance, and introducing another metal to form Cu–alloy can modulate all the above factors. Cu-based bimetallic nanoclusters have demonstrated unusual properties and extraordinary catalytic capabilities [90, 184], yet controlling the number and the exact position of a foreign metal atom remains challenging [163, 185]. Particularly, single-metal-atom doping have been gaining tremendous efforts in catalysis study but increasing the production yield for generating single-atom doping during the synthetic process, understanding the geometric and electronic structure change in the on-working catalytic process is essential for future high-performance catalyst design [186–189].
4. *In situ* reaction mechanism study. Understanding the reaction mechanism in on-working status is quite valuable but still challenging. The *in situ* and *operando* spectroscopic and synchronous techniques such as surface enhanced Raman scattering, infrared spectroscopy, high-energy X-ray diffraction (HE-XRD), extended X-ray absorption fine structure (EXAFS), X-ray absorption near edge structure (XANES), and small-angle neutron scattering (SANS) can provide the possibility of acquiring the structure of the catalytic intermediates, which can enhance the evidence for proposed reaction mechanism [190–193]. For instance, the *in situ* infrared spectroscopy was employed to capture the reaction intermediates during the electrocatalytic nitrate reduction catalyzed by $Ag_{30}Pd_4$ nanoclusters; hence, the tandem catalytic mechanism was successfully revealed by our group [93]. Nevertheless, the consecutive picture of the whole reaction process including adsorption, transfer, desorption of the reaction intermediates on Cu nanoclusters are quite limited in current studies, and more advanced *in situ/operando* study and the necessary instrumental modification for some specific *in situ/operando* investigations are expected.
5. The more precise theoretical simulations. Theoretical simulations can calculate the energy barrier of each step, acquire the optimal configuration between the cluster and the reactant, the intermediate, or the product, hence plays a critical role in speculating the active sites and deciding the rate-determining step [104]. However, the accuracy of these calculations depends on the authenticity and the extent of the structure proximity between the real crystal structure and the theoretical model. The fully ligand capped Cu nanoclusters are too complicated to build a real model, so the "ligand simplification" strategy is widely used. For instance, $Au_{25}(SCH_3)_{18}$ has been used to replace $Au_{25}(SC_2H_4Ph)_{18}$, $Au_{25}(SC_6H_{13})_{18}$ and $Au_{25}(SC_{12}H_{25})_{18}$ in several cases for building theoretical models [194–196]. Authentic models can help to understand the true reaction process and gain more realistic reaction mechanism but given the complexity of the cluster structures and the reaction conditions, more precise and realistic theoretical simulations still have a long way to go.

https://doi.org/10.1007/s40820-024-01555-6

Acknowledgements The study is supported by the open funds of Key Laboratory of Functional Inorganic Material Chemistry (Heilongjiang University), Ministry of Education, China. Z. T. acknowledges the funding from Guangdong Natural Science Funds (No. 2023A0505050107).

Author Contributions MC contributed to the investigation and original draft writing. CG, LQ, LW, LQ, and KC were involved in the literature search and formal analysis. ZT performed the funding acquisition and draft finalization.

Declarations

Conflict of interest The authors declare no conflict of interest. They have no known competing financial interests or personal relationships that could have appeared to influence the work reported in this paper.

References

1. R. Jin, C. Zeng, M. Zhou, Y. Chen, Atomically precise colloidal metal nanoclusters and nanoparticles: fundamentals and opportunities. Chem. Rev. **116**, 10346–10413 (2016). https://doi.org/10.1021/acs.chemrev.5b00703
2. Y. Lv, T. Jiang, Q. Zhang, H. Yu, M. Zhu, Recent progress in atomically precise Ag/Cu-based hydride clusters. Polyoxometalates **3**, 9140050 (2024). https://doi.org/10.26599/pom.2023.9140050
3. X.-M. Luo, Y.-K. Li, X.-Y. Dong, S.-Q. Zang, Platonic and Archimedean solids in discrete metal-containing clusters. Chem. Soc. Rev. **52**, 383–444 (2023). https://doi.org/10.1039/d2cs00582d
4. R.W. Murray, Nanoelectrochemistry: metal nanoparticles, nanoelectrodes, and nanopores. Chem. Rev. **108**, 2688–2720 (2008). https://doi.org/10.1021/cr068077e
5. P.D. Jadzinsky, G. Calero, C.J. Ackerson, D.A. Bushnell, R.D. Kornberg, Structure of a thiol monolayer-protected gold nanoparticle at 1.1 A resolution. Science **318**, 430–433 (2007). https://doi.org/10.1126/science.1148624
6. L. Shang, J. Xu, G. Nienhaus, Recent advances in synthesizing metal nanocluster-based nanocomposites for application in sensing, imaging and catalysis. Nano Today **28**, 100767 (2019). https://doi.org/10.1016/j.nantod.2019.100767
7. S. Qian, Z. Wang, Z. Zuo, X. Wang, Q. Wang et al., Engineering luminescent metal nanoclusters for sensing applications. Coord. Chem. Rev. **451**, 214268 (2022). https://doi.org/10.1016/j.ccr.2021.214268
8. Y. Jin, C. Zhang, X.-Y. Dong, S.-Q. Zang, T.C.W. Mak, Shell engineering to achieve modification and assembly of atomically-precise silver clusters. Chem. Soc. Rev. **50**, 2297–2319 (2021). https://doi.org/10.1039/d0cs01393e
9. Q. Yao, L. Liu, S. Malola, M. Ge, H. Xu et al., Supercrystal engineering of atomically precise gold nanoparticles promoted by surface dynamics. Nat. Chem. **15**, 230–239 (2023). https://doi.org/10.1038/s41557-022-01079-9
10. W. Jing, H. Shen, R. Qin, Q. Wu, K. Liu et al., Surface and interface coordination chemistry learned from model heterogeneous metal nanocatalysts: from atomically dispersed catalysts to atomically precise clusters. Chem. Rev. **123**, 5948–6002 (2023). https://doi.org/10.1021/acs.chemrev.2c00569
11. M.S. Bootharaju, C.W. Lee, G. Deng, H. Kim, K. Lee et al., Atom-precise heteroatom core-tailoring of nanoclusters for enhanced solar hydrogen generation. Adv. Mater. **35**, e2207765 (2023). https://doi.org/10.1002/adma.202207765
12. H. Shan, J. Shi, T. Chen, Y. Cao, Q. Yao et al., Modulating catalytic activity and stability of atomically precise gold nanoclusters as peroxidase mimics *via* ligand engineering. ACS Nano **17**, 2368–2377 (2023). https://doi.org/10.1021/acsnano.2c09238
13. Y.-S.Chen, H. Choi, P.V. Kamat, Metal-cluster-sensitized solar cells. A new class of thiolated gold sensitizers delivering efficiency greater than 2%. J. Am. Chem. Soc. **135**, 8822–8825 (2013). https://doi.org/10.1021/ja403807f
14. Y.-S. Chen, P.V. Kamat, Glutathione-capped gold nanoclusters as photosensitizers. Visible light-induced hydrogen generation in neutral water. J. Am. Chem. Soc. **136**, 6075–6082 (2014). https://doi.org/10.1021/ja5017365
15. B. Du, X. Jiang, A. Das, Q. Zhou, M. Yu et al., Glomerular barrier behaves as an atomically precise bandpass filter in a sub-nanometre regime. Nat. Nanotechnol. **12**, 1096–1102 (2017). https://doi.org/10.1038/nnano.2017.170
16. Y. Hua, J.-H. Huang, Z.-H. Shao, X.-M. Luo, Z.-Y. Wang et al., Composition-dependent enzyme mimicking activity and radiosensitizing effect of bimetallic clusters to modulate tumor hypoxia for enhanced cancer therapy. Adv. Mater. **34**, 2203734 (2022). https://doi.org/10.1002/adma.202203734
17. T.-T. Jia, G. Yang, S.-J. Mo, Z.-Y. Wang, B.-J. Li et al., Atomically precise gold–levonorgestrel nanocluster as a radiosensitizer for enhanced cancer therapy. ACS Nano **13**, 8320–8328 (2019). https://doi.org/10.1021/acsnano.9b03767
18. M. Walter, J. Akola, O. Lopez-Acevedo, P.D. Jadzinsky, G. Calero et al., A unified view of ligand-protected gold clusters as superatom complexes. Proc. Natl. Acad. Sci. U.S.A. **105**, 9157–9162 (2008). https://doi.org/10.1073/pnas.0801001105
19. M.G. Taylor, G. Mpourmpakis, Thermodynamic stability of ligand-protected metal nanoclusters. Nat. Commun. **8**, 15988 (2017). https://doi.org/10.1038/ncomms15988

20. S.-Y. Kang, Z.-A. Nan, Q.-M. Wang, Superatomic orbital splitting in coinage metal nanoclusters. J. Phys. Chem. Lett. **13**, 291–295 (2022). https://doi.org/10.1021/acs.jpclett.1c03563
21. J.D. Schneider, B.A. Smith, G.A. Williams, D.R. Powell, F. Perez et al., Synthesis and characterization of Cu(II) and mixed-valence Cu(I)Cu(II) clusters supported by pyridylamide ligands. Inorg. Chem. **59**, 5433–5446 (2020). https://doi.org/10.1021/acs.inorgchem.0c00008
22. L.L.-M. Zhang, W.-Y. Wong, Atomically precise copper nanoclusters as ultrasmall molecular aggregates: appealing compositions, structures, properties, and applications. Aggregate **4**, e266 (2023). https://doi.org/10.1002/agt2.266
23. J. Sang, P. Wei, T. Liu, H. Lv, X. Ni et al., A reconstructed $Cu_2P_2O_7$ catalyst for selective CO_2 electroreduction to multicarbon products. Angew. Chem. Int. Ed. **61**, e202114238 (2022). https://doi.org/10.1002/anie.202114238
24. C. Sun, K. Liu, J. Zhang, Q. Liu, X.J. Liu et al., In situ transmission electron microscopy and three-dimensional electron tomography for catalyst studies. Chin. J. Struct. Chem. **41**, 2210056–2210076 (2022). https://doi.org/10.14102/j.cnki.0254-5861.2022-0187
25. H. Sun, L. Lin, W. Hua, X. Xie, Q. Mu et al., Atomically dispersed Co−Cu alloy reconstructed from metal-organic framework to promote electrochemical CO_2 methanation. Nano Res. **16**, 3680–3686 (2023). https://doi.org/10.1007/s12274-022-4728-1
26. X. Gong, Z.-H. Liu, Q. Xu, L. Wang, Q. Guo et al., Single-molecule manipulation of copper nanoclusters for modulating nonlinear optics. Polyoxometalates **4**, 9140072 (2025). https://doi.org/10.26599/pom.2024.9140072
27. Q.-J. Wu, D.-H. Si, P.-P. Sun, Y.-L. Dong, S. Zheng et al., Atomically precise copper nanoclusters for highly efficient electroreduction of CO_2 towards hydrocarbons *via* breaking the coordination symmetry of Cu site. Angew. Chem. Int. Ed. **62**, e202306822 (2023). https://doi.org/10.1002/anie.202306822
28. S. Zhao, N. Austin, M. Li, Y. Song, S.D. House et al., Influence of atomic-level morphology on catalysis: the case of sphere and rod-like gold nanoclusters for CO_2 electroreduction. ACS Catal. **8**, 4996–5001 (2018). https://doi.org/10.1021/acscatal.8b00365
29. L. Qin, F. Sun, X. Ma, G. Ma, Y. Tang et al., Homoleptic alkynyl-protected Ag_{15} nanocluster with atomic precision: structural analysis and electrocatalytic performance toward CO_2 reduction. Angew. Chem. Int. Ed. **60**, 26136–26141 (2021). https://doi.org/10.1002/anie.202110330
30. X.-K. Wan, J.-Q. Wang, Q.-M. Wang, Ligand-protected au_{55} with a novel structure and remarkable CO_2 electroreduction performance. Angew. Chem. Int. Ed. **60**, 20748–20753 (2021). https://doi.org/10.1002/anie.202108207
31. S.-F. Yuan, R.-L. He, X.-S. Han, J.-Q. Wang, Z.-J. Guan et al., Robust gold nanocluster protected with amidinates for electrocatalytic CO_2 reduction. Angew. Chem. Int. Ed. **60**, 14345–14349 (2021). https://doi.org/10.1002/anie.202103060
32. L. Chen, F. Sun, Q. Shen, L. Qin, Y. Liu et al., Homoleptic alkynyl-protected Ag_{32} nanocluster with atomic precision: probing the ligand effect toward CO_2 electroreduction and 4-nitrophenol reduction. Nano Res. **15**, 8908–8913 (2022). https://doi.org/10.1007/s12274-022-4812-6
33. J. Wang, F. Xu, Z.-Y. Wang, S.-Q. Zang, T.C.W. Mak, Ligand-shell engineering of a Au_{28} nanocluster boosts electrocatalytic CO_2 reduction. Angew. Chem. Int. Ed. **61**, e202207492 (2022). https://doi.org/10.1002/anie.202207492
34. S. Li, A.V. Nagarajan, X. Du, Y. Li, Z. Liu et al., Dissecting critical factors for electrochemical CO_2 reduction on atomically precise Au nanoclusters. Angew. Chem. Int. Ed. **61**, e202211771 (2022). https://doi.org/10.1002/anie.202211771
35. T.-A D. Nguyen, Z.R. Jones, D.F. Leto, G. Wu, S.L. Scott et al., Ligand-exchange-induced growth of an atomically precise Cu_{29} nanocluster from a smaller cluster. Chem. Mater. **28**, 8385–8390 (2016). https://doi.org/10.1021/acs.chemmater.6b03879
36. A.W. Cook, Z.R. Jones, G. Wu, S.L. Scott, T.W. Hayton, An organometallic Cu_{20} nanocluster: synthesis, characterization, immobilization on silica, and click chemistry. J. Am. Chem. Soc. **140**, 394–400 (2018). https://doi.org/10.1021/jacs.7b10960
37. M. Qu, F.-Q. Zhang, D.-H. Wang, H. Li, J.-J. Hou et al., Observation of non-FCC copper in alkynyl-protected Cu_{53} nanoclusters. Angew. Chem. Int. Ed. **59**, 6507–6512 (2020). https://doi.org/10.1002/anie.202001185
38. S. Li, X. Yan, J. Tang, D. Cao, X. Sun et al., Cu_{26} nanoclusters with quintuple ligand shells for CO_2 electrocatalytic reduction. Chem. Mater. **35**, 6123–6132 (2023). https://doi.org/10.1021/acs.chemmater.3c01247
39. S. Lee, M.S. Bootharaju, G. Deng, S. Malola, W. Baek et al., $Cu_{32}(PET)_{24}H_8Cl_2](PPh_4)_2$: a copper hydride nanocluster with a bisquare antiprismatic core. J. Am. Chem. Soc. **142**, 13974–13981 (2020). https://doi.org/10.1021/jacs.0c06577
40. T.-A D. Nguyen, Z.R. Jones, B.R. Goldsmith, W.R. Buratto, G. Wu et al., A Cu_{25} nanocluster with partial Cu(0) character. J. Am. Chem. Soc. **137**, 13319–13324 (2015). https://doi.org/10.1021/jacs.5b07574
41. N. Zhang, Y. Li, S. Han, Y. Wei, H. Hu et al., Cluster light-emitting diodes containing copper iodine cube with 100% exciton utilization using host-cluster synergy. Angew. Chem. Int. Ed. **62**, e202305018 (2023). https://doi.org/10.1002/anie.202305018
42. A.K. Das, S. Biswas, V.S. Wani, A.S. Nair, B. Pathak et al., $Cu_{18}H_3(S\text{-}adm)_{12}(PPh_3)_4Cl_2]$: fusion of Platonic and *Johnson* solids through a Cu(0) center and its photophysical properties. Chem. Sci. **13**, 7616–7625 (2022). https://doi.org/10.1039/d2sc02544b
43. T. Jia, Z.-J. Guan, C. Zhang, X.-Z. Zhu, Y.-X. Chen et al., Eight-electron superatomic Cu_{31} nanocluster with chiral kernel and NIR-II emission. J. Am. Chem. Soc. **145**, 10355–10363 (2023). https://doi.org/10.1021/jacs.3c02215
44. X.-Z. Zhu, T. Jia, Z.-J. Guan, Q. Zhang, Y. Yang, Elongation of a trigonal-prismatic copper cluster by diphosphine ligands

 https://doi.org/10.1007/s40820-024-01555-6

with longer spacers. Inorg. Chem. **61**, 15144–15151 (2022). https://doi.org/10.1021/acs.inorgchem.2c02306

45. J. Sun, X. Tang, Z.-H. Liu, Z. Xie, B. Yan et al., Labile ligands protected Cu_{50} nanoclusters with tailorable optical limiting effect. ACS Mater. Lett. **6**, 281–289 (2024). https://doi.org/10.1021/acsmaterialslett.3c01305
46. J. Sun, X. Tang, X. Yan, W. Jing, Z. Xie et al., Atomically precise Cu_{41} clusters as model catalysts: open metal sites matter. Next Mater. **3**, 100091 (2024). https://doi.org/10.1016/j.nxmate.2023.100091
47. B.-L. Han, Z. Liu, L. Feng, Z. Wang, R.K. Gupta et al., Polymorphism in atomically precise Cu_{23} nanocluster incorporating tetrahedral$[Cu_4]^0$ kernel. J. Am. Chem. Soc. **142**, 5834–5841 (2020). https://doi.org/10.1021/jacs.0c01053
48. P. Yuan, R. Chen, X. Zhang, F. Chen, J. Yan et al., Ether-soluble Cu_{53} nanoclusters as an effective precursor of high-quality CuI films for optoelectronic applications. Angew. Chem. Int. Ed. **58**, 835–839 (2019). https://doi.org/10.1002/anie.201812236
49. C. Zhang, Z. Wang, W.-D. Si, L. Wang, J.-M. Dou et al., Solvent-induced isomeric Cu_{13} nanoclusters: chlorine to copper charge transfer boosting molecular oxygen activation in sulfide selective oxidation. ACS Nano **16**, 9598–9607 (2022). https://doi.org/10.1021/acsnano.2c02885
50. L. Qin, G. Ma, L. Wang, Z. Tang, Atomically precise metal nanoclusters for (photo)electroreduction of CO_2: recent advances, challenges and opportunities. J. Energy Chem. **57**, 359–370 (2021). https://doi.org/10.1016/j.jechem.2020.09.003
51. Q. Tang, Y. Lee, D.-Y. Li, W. Choi, C.W. Liu et al., Lattice-hydride mechanism in electrocatalytic CO_2 reduction by structurally precise copper-hydride nanoclusters. J. Am. Chem. Soc. **139**, 9728–9736 (2017). https://doi.org/10.1021/jacs.7b05591
52. L.-J. Liu, Z.-Y. Wang, Z.-Y. Wang, R. Wang, S.-Q. Zang et al., Mediating CO_2 electroreduction activity and selectivity over atomically precise copper clusters. Angew. Chem. Int. Ed. **61**, e202205626 (2022). https://doi.org/10.1002/anie.202205626
53. J. Wang, J. Cai, K.-X. Ren, L. Liu, S.-J. Zheng et al., Stepwise structural evolution toward robust carboranealkynyl-protected copper nanocluster catalysts for nitrate electroreduction. Sci. Adv. **10**, eadn7556 (2024). https://doi.org/10.1126/sciadv.adn7556
54. J.-P. Dong, Y. Xu, X.-G. Zhang, H. Zhang, L. Yao et al., Copper-sulfur-nitrogen cluster providing a local proton for efficient carbon dioxide photoreduction. Angew. Chem. Int. Ed. **62**, e202313648 (2023). https://doi.org/10.1002/anie.202313648
55. A. Sagadevan, A. Ghosh, P. Maity, O.F. Mohammed, O.M. Bakr et al., Visible-light copper nanocluster catalysis for the C-N coupling of aryl chlorides at room temperature. J. Am. Chem. Soc. **144**, 12052–12061 (2022). https://doi.org/10.1021/jacs.2c02218
56. G.-G. Luo, Z.-H. Pan, B.-L. Han, G.-L. Dong, C.-L. Deng et al., Total structure, electronic structure and catalytic hydrogenation activity of metal-deficient chiral polyhydride Cu_{57} nanoclusters. Angew. Chem. Int. Ed. **62**, e202306849 (2023). https://doi.org/10.1002/anie.202306849
57. C. Dong, R.-W. Huang, A. Sagadevan, P. Yuan, L. Gutiérrez-Arzaluz et al., Isostructural nanocluster manipulation reveals pivotal role of one surface atom in click chemistry. Angew. Chem. Int. Ed. **62**, e202307140 (2023). https://doi.org/10.1002/anie.202307140
58. S. Nematulloev, A. Sagadevan, B. Alamer, A. Shkurenko, R. Huang et al., Atomically precise defective copper nanocluster catalysts for highly selective C-C cross-coupling reactions. Angew. Chem. Int. Ed. **62**, e202303572 (2023). https://doi.org/10.1002/anie.202303572
59. S. Biswas, A. Pal, M.K. Jena, S. Hossain, S. Jin et al., Luminescent hydride-free$[Cu_7(SC_5H_9)_7(PPh_3)_3]$nanocluster: facilitating highly selective C-C bond formation. J. Am. Chem. Soc. **146**, 20937–20944 (2024). https://doi.org/10.1021/jacs.4c05678
60. T. Jia, Y.-X. Li, X.-H. Ma, M.-M. Zhang, X.-Y. Dong et al., Atomically precise ultrasmall copper cluster for room-temperature highly regioselective dehydrogenative coupling. Nat. Commun. **14**, 6877 (2023). https://doi.org/10.1038/s41467-023-42688-3
61. X. Xu, Y. Liu, F. Sun, Y. Jia, Q. Xu et al., Array-based clusters of copper with largely exposed metal sites for promoting catalysis. Chem. Mater. **35**, 7588–7596 (2023). https://doi.org/10.1021/acs.chemmater.3c01277
62. Y.-M. Wang, X.-C. Lin, K.-M. Mo, M. Xie, Y.-L. Huang et al., An atomically precise pyrazolate-protected copper nanocluster exhibiting exceptional stability and catalytic activity. Angew. Chem. Int. Ed. **62**, e202218369 (2023). https://doi.org/10.1002/anie.202218369
63. G. Dong, Z. Pan, B. Han, Y. Tao, X. Chen et al., Multilayer 3D chirality and double-helical assembly in a copper nanocluster with a triple-helical Cu_{15} core. Angew. Chem. Int. Ed. **62**, e202302595 (2023). https://doi.org/10.1002/anie.202302595
64. X. Sun, Y. Wang, Q. Wu, Y.-Z. Han, X. Gong et al., Cu_{66} nanoclusters from hierarchical square motifs: synthesis, assembly, and catalysis. Aggregate, e651 (2024). https://doi.org/10.1002/agt2.651
65. C.-Y. Liu, T.-Y. Liu, Z.-J. Guan, S. Wang, Y.-Y. Dong et al., Dramatic difference between $Cu_{20}H_8$ and $Cu_{20}H_9$ Clusters in catalysis. CCS Chem. **6**, 1581–1590 (2024). https://doi.org/10.31635/ccschem.023.202303448
66. B. Yan, X. You, X. Tang, J. Sun, Q. Xu et al., Carboxylate-protected "isostructural" Cu_{20} nanoclusters as a model system: carboxylate effect on controlling catalysis. Chem. Mater. **36**, 1004–1012 (2024). https://doi.org/10.1021/acs.chemmater.3c03131
67. Y. Li, R. Jin, Seeing ligands on nanoclusters and in their assemblies by X-ray crystallography: atomically precise nanochemistry and beyond. J. Am. Chem. Soc. **142**, 13627–13644 (2020). https://doi.org/10.1021/jacs.0c05866
68. B. Zhang, J. Chen, Y. Cao, O.J.H. Chai, J. Xie, Ligand design in ligand-protected gold nanoclusters. Small **17**, e2004381 (2021). https://doi.org/10.1002/smll.202004381

69. Z.-J. Guan, R.-L. He, S.-F. Yuan, J.-J. Li, F. Hu et al., Ligand engineering toward the trade-off between stability and activity in cluster catalysis. Angew. Chem. Int. Ed. **61**, e202116965 (2022). https://doi.org/10.1002/anie.202116965
70. W. Fei, Y. Tao, Y. Qiao, S.-Y. Tang, M.-B. Li, Structural modification and performance regulation of atomically precise metal nanoclusters by phosphine. Polyoxometalates **2**, 9140043 (2023). https://doi.org/10.26599/pom.2023.9140043
71. S.-F. Yuan, W.-D. Liu, C.-Y. Liu, Z.-J. Guan, Q.-M. Wang, Nitrogen donor protection for atomically precise metal nanoclusters. Chemistry **28**, e202104445 (2022). https://doi.org/10.1002/chem.202104445
72. Z. Lei, X.-K. Wan, S.-F. Yuan, Z.-J. Guan, Q.-M. Wang, Alkynyl approach toward the protection of metal nanoclusters. Acc. Chem. Res. **51**, 2465–2474 (2018). https://doi.org/10.1021/acs.accounts.8b00359
73. L. Chen, L. Wang, Q. Shen, Y. Liu, Z. Tang, All-alkynyl-protected coinage metal nanoclusters: from synthesis to electrocatalytic CO_2 reduction applications. Mater. Chem. Front. **7**, 1482–1495 (2023). https://doi.org/10.1039/d2qm01282k
74. R.W. Huang, J. Yin, C. Dong, A. Ghosh, M.J. Alhilaly et al., $Cu_{81}(PhS)_{46}(^tBuNH_2)_{10}(H)_{32}]^{3+}$ reveals the coexistence of large planar cores and hemispherical shells in high-nuclearity copper nanoclusters. J. Am. Chem. Soc. **142**, 8696–8705 (2020). https://doi.org/10.1021/jacs.0c00541
75. P.-P. Sun, B.-L. Han, H.-G. Li, C.-K. Zhang, X. Xin et al., Real-time fluorescent monitoring of kinetically controlled supramolecular self-assembly of atom-precise Cu_8 nanocluster. Angew. Chem. Int. Ed. **61**, e202200180 (2022). https://doi.org/10.1002/anie.202200180
76. Q.-Q. Huang, M.-Y. Hu, Y.-L. Li, N.-N. Chen, Y. Li et al., Novel ultrabright luminescent copper nanoclusters and application in light-emitting devices. Chem. Commun. **57**, 9890–9893 (2021). https://doi.org/10.1039/d1cc03799d
77. M.K. Osei, S. Mirzaei, X. Bogetti, E. Castro, M.A. Rahman et al., Synthesis of square planar Cu_4 clusters. Angew. Chem. Int. Ed. **61**, e202209529 (2022). https://doi.org/10.1002/anie.202209529
78. C.-Y. Liu, S.-F. Yuan, S. Wang, Z.-J. Guan, D.-E. Jiang et al., Structural transformation and catalytic hydrogenation activity of amidinate-protected copper hydride clusters. Nat. Commun. **13**, 2082 (2022). https://doi.org/10.1038/s41467-022-29819-y
79. H.-Y. Zhuo, H.-F. Su, Z.-Z. Cao, W. Liu, S.-A. Wang et al., High-nuclear organometallic copper(I)-alkynide clusters: thermochromic near-infrared luminescence and solution stability. Chemistry **22**, 17619–17626 (2016). https://doi.org/10.1002/chem.201603797
80. M.-M. Zhang, X.-Y. Dong, Z.-Y. Wang, H.-Y. Li, S.-J. Li et al., AIE triggers the circularly polarized luminescence of atomically precise enantiomeric copper(I) alkynyl clusters. Angew. Chem. Int. Ed. **59**, 10052–10058 (2020). https://doi.org/10.1002/anie.201908909
81. M. Brust, M. Walker, D. Bethell, D.J. Schiffrin, R. Whyman, Synthesis of thiol-derivatised gold nanoparticles in a two-phase Liquid–Liquid system. J. Chem. Soc., Chem. Commun., 801–802 (1994). https://doi.org/10.1039/c39940000801
82. M. Brust, J. Fink, D. Bethell, D.J. Schiffrin, C. Kiely, Synthesis and reactions of functionalised gold nanoparticles. J. Chem. Soc., Chem. Commun., 1655 (1995). https://doi.org/10.1039/c39950001655
83. R. Jin, H. Qian, Z. Wu, Y. Zhu, M. Zhu et al., Size focusing: a methodology for synthesizing atomically precise gold nanoclusters. J. Phys. Chem. Lett. **1**, 2903–2910 (2010). https://doi.org/10.1021/jz100944k
84. Q. Yao, T. Chen, X. Yuan, J. Xie, Toward total synthesis of thiolate-protected metal nanoclusters. Acc. Chem. Res. **51**, 1338–1348 (2018). https://doi.org/10.1021/acs.accounts.8b00065
85. X. Yuan, L.L. Chng, J. Yang, J.Y. Ying, Miscible-solvent-assisted two-phase synthesis of monolayer-ligand-protected metal nanoclusters with various sizes. Adv. Mater. **32**, e1906063 (2020). https://doi.org/10.1002/adma.201906063
86. Z. Wang, X. Pan, S. Qian, G. Yang, F. Du et al., The beauty of binary phases: a facile strategy for synthesis, processing, functionalization, and application of ultrasmall metal nanoclusters. Coord. Chem. Rev. **438**, 213900 (2021). https://doi.org/10.1016/j.ccr.2021.213900
87. Y. Li, M. Zhou, R. Jin, Programmable metal nanoclusters with atomic precision. Adv. Mater. **33**, e2006591 (2021). https://doi.org/10.1002/adma.202006591
88. X. Ma, G. Ma, L. Qin, G. Chen, S. Chen et al., A synchronous nucleation and passivation strategy for controllable synthesis of $Au_{36}(PA)_{24}$: unveiling the formation process and the role of $Au_{22}(PA)_{18}$ intermediate. Sci. China Chem. **63**, 1777–1784 (2020). https://doi.org/10.1007/s11426-020-9819-4
89. X. Ma, Z. Tang, L. Qin, J. Peng, L. Li et al., Unravelling the formation mechanism of alkynyl protected gold clusters: a case study of phenylacetylene stabilized Au_{144} molecules. Nanoscale **12**, 2980–2986 (2020). https://doi.org/10.1039/c9nr10930g
90. X. Ma, F. Sun, L. Qin, Y. Liu, X. Kang et al., Electrochemical CO_2 reduction catalyzed by atomically precise alkynyl-protected Au_7Ag_8, Ag_9Cu_6, and $Au_2Ag_8Cu_5$ nanoclusters: probing the effect of multi-metal core on selectivity. Chem. Sci. **13**, 10149–10158 (2022). https://doi.org/10.1039/d2sc02886g
91. Y. Tang, F. Sun, X. Ma, L. Qin, G. Ma et al., Alkynyl and halogen co-protected $(AuAg)_{44}$ nanoclusters: a comparative study on their optical absorbance, structure, and hydrogen evolution performance. Dalton Trans. **51**, 7845–7850 (2022). https://doi.org/10.1039/d2dt00634k
92. G. Ma, Y. Tang, L. Chen, L. Qin, Q. Shen et al., A homoleptic alkynyl-protected $Au(I)_9$-$Ag(I)_9$ cluster: structure analysis, optical properties, and catalytic implications. Eur. J. Inorg. Chem. **2022**, e202200176 (2022). https://doi.org/10.1002/ejic.202200176

 https://doi.org/10.1007/s40820-024-01555-6

93. L. Qin, F. Sun, Z. Gong, G. Ma, Y. Chen et al., Electrochemical NO_3^- reduction catalyzed by atomically precise $Ag_{30}Pd_4$ bimetallic nanocluster: synergistic catalysis or tandem catalysis? ACS Nano **17**, 12747–12758 (2023). https://doi.org/10.1021/acsnano.3c03692
94. L. Chen, F. Sun, Q. Shen, L. Wang, Y. Liu et al., Structure, optical properties, and catalytic applications of alkynyl-protected M_4Rh_2 (M = Ag/Au) nanoclusters with atomic precision: a comparative study. Dalton Trans. **52**, 9441–9447 (2023). https://doi.org/10.1039/d3dt01326j
95. L. Wang, L. Chen, L. Qin, Y. Liu, Z. Tang, Alkynyl-protected $Ag_{20}Rh_2$ nanocluster with atomic precision: structure analysis and tri-functionality catalytic application. Chem. Asian J. **18**, e202300685 (2023). https://doi.org/10.1002/asia.202300685
96. X. Ma, Y. Tang, G. Ma, L. Qin, Z. Tang, Controllable synthesis and formation mechanism study of homoleptic alkynyl-protected Au nanoclusters: recent advances, grand challenges, and great opportunities. Nanoscale **13**, 602–614 (2021). https://doi.org/10.1039/d0nr07499c
97. X. Yuan, B. Zhang, Z. Luo, Q. Yao, D.T. Leong et al., Balancing the rate of cluster growth and etching for gram-scale synthesis of thiolate-protected Au_{25} nanoclusters with atomic precision. Angew. Chem. Int. Ed. **53**, 4623–4627 (2014). https://doi.org/10.1002/anie.201311177
98. Z. Wu, J. Suhan, R. Jin, One-pot synthesis of atomically monodisperse, thiol-functionalized Au_{25}nanoclusters. J. Mater. Chem. **19**, 622–626 (2009). https://doi.org/10.1039/b815983a
99. A.C. Dharmaratne, T. Krick, A. Dass, Nanocluster size evolution studied by mass spectrometry in room temperature $Au_{25}(SR)_{18}$ synthesis. J. Am. Chem. Soc. **131**, 13604–13605 (2009). https://doi.org/10.1021/ja906087a
100. S. Ito, S. Takano, T. Tsukuda, Alkynyl-protected $Au_{22}(C{\equiv}CR)_{18}$ clusters featuring new interfacial motifs and R-dependent photoluminescence. J. Phys. Chem. Lett. **10**, 6892–6896 (2019). https://doi.org/10.1021/acs.jpclett.9b02920
101. Z.-J. Guan, F. Hu, J.-J. Li, Z.-R. Wen, Y.-M. Lin et al., Isomerization in alkynyl-protected gold nanoclusters. J. Am. Chem. Soc. **142**, 2995–3001 (2020). https://doi.org/10.1021/jacs.9b11836
102. Y.-J. Zhong, J.-H. Liao, T.-H. Chiu, S. Kahlal, C.-J. Lin et al., A two-electron silver superatom isolated from thermally induced internal redox reaction of A silver(I) hydride. Angew. Chem. Int. Ed. **60**, 12712–12716 (2021). https://doi.org/10.1002/anie.202100965
103. K.K. Chakrahari, J.H. Liao, S. Kahlal, Y.C. Liu, M.H. Chiang et al., $Cu_{13}\{S_2\ CN^n\ Bu_2\}_6$ (acetylide)$_4]^+$: a two-electron superatom. Angew. Chem. Int. Ed. **55**, 14704–14708 (2016). https://doi.org/10.1002/anie.201608609
104. F. Sun, Q. Tang, D-e. Jiang Theoretical advances in understanding and designing the active sites for hydrogen evolution reaction. ACS Catal. **12**, 8404–8433 (2022). https://doi.org/10.1021/acscatal.2c02081
105. Y. Wang, X. Zheng, D. Wang, Design concept for electrocatalysts. Nano Res. **15**, 1730–1752 (2022). https://doi.org/10.1007/s12274-021-3794-0
106. X.L. Tian, J.Y. Li, L.X. Zhang, Y. Chen, Structural chemistry in energy relevant-catalysis reaction. Chin. J. Struct. Chem. **41**, 2207001–2207001 (2022). https://doi.org/10.14102/j.cnki.0254-5861.2022-0160
107. Z.W. Seh, J. Kibsgaard, C.F. Dickens, I. Chorkendorff, J.K. Nørskov et al., Combining theory and experiment in electrocatalysis: insights into materials design. Science **355**, eaad4998 (2017). https://doi.org/10.1126/science.aad4998
108. O.S. Bushuyev, P. De Luna, C.T. Dinh, L. Tao, G. Saur et al., What should we make with CO_2 and how can we make it? Joule **2**, 825–832 (2018). https://doi.org/10.1016/j.joule.2017.09.003
109. M. Lu, M. Zhang, J. Liu, Y. Chen, J.-P. Liao et al., Covalent organic framework based functional materials: important catalysts for efficient CO_2 utilization. Angew. Chem. Int. Ed. **61**, e202200003 (2022). https://doi.org/10.1002/anie.202200003
110. Y. Quan, J. Zhu, G. Zheng, Electrocatalytic reactions for converting CO_2 to value-added products. Small Sci. **1**, 2100043 (2021). https://doi.org/10.1002/smsc.202100043
111. Y. Li, T.-B. Lu, Coupling electrochemical CO_2 reduction with value-added anodic oxidation reactions: progress and challenges. Mater. Chem. Front. **8**, 341–353 (2024). https://doi.org/10.1039/d3qm00625e
112. G. Ma, L. Qin, Y. Liu, H. Fan, L. Qiao et al., A review of CO_2 reduction reaction catalyzed by atomical-level Ag nanomaterials: atom-precise nanoclusters and atomically dispersed catalysts. Surf. Interfaces **36**, 102555 (2023). https://doi.org/10.1016/j.surfin.2022.102555
113. G. Wang, J. Chen, Y. Ding, P. Cai, L. Yi et al., Electrocatalysis for CO_2 conversion: from fundamentals to value-added products. Chem. Soc. Rev. **50**, 4993–5061 (2021). https://doi.org/10.1039/d0cs00071j
114. H. Liu, Y. Zhu, J. Ma, Z. Zhang, W. Hu, Atomically thin catalysts: recent advances in atomic-level engineering of nanostructured catalysts for electrochemical CO_2 reduction. Adv. Funct. Mater. **30**, 2070107 (2020). https://doi.org/10.1002/adfm.202070107
115. B. Pan, Y. Wang, Y. Li, Understanding and leveraging the effect of cations in the electrical double layer for electrochemical CO_2 reduction. Chem Catal. **2**, 1267–1276 (2022). https://doi.org/10.1016/j.checat.2022.03.012
116. L. Zhou, R. Lv, Rational catalyst design and interface engineering for electrochemical CO_2 reduction to high-valued alcohols. J. Energy Chem. **70**, 310–331 (2022). https://doi.org/10.1016/j.jechem.2022.02.033
117. S. Ji, Y. Chen, X. Wang, Z. Zhang, D. Wang et al., Chemical synthesis of single atomic site catalysts. Chem. Rev. **120**, 11900–11955 (2020). https://doi.org/10.1021/acs.chemrev.9b00818
118. J. Duan, T. Liu, Y. Zhao, R. Yang, Y. Zhao et al., Active and conductive layer stacked superlattices for highly selective

CO_2 electroreduction. Nat. Commun. **13**, 2039 (2022). https://doi.org/10.1038/s41467-022-29699-2

119. Y. Zheng, A. Vasileff, X. Zhou, Y. Jiao, M. Jaroniec et al., Understanding the roadmap for electrochemical reduction of CO_2 to multi-carbon oxygenates and hydrocarbons on copper-based catalysts. J. Am. Chem. Soc. **141**, 7646–7659 (2019). https://doi.org/10.1021/jacs.9b02124
120. J. Wang, H.-Y. Tan, Y. Zhu, H. Chu, H.M. Chen, Linking the dynamic chemical state of catalysts with the product profile of electrocatalytic CO_2 reduction. Angew. Chem. Int. Ed. **60**, 17254–17267 (2021). https://doi.org/10.1002/anie.202017181
121. S. Liu, B. Zhang, L. Zhang, J. Sun, Rational design strategies of Cu-based electrocatalysts for CO_2 electroreduction to C2 products. J. Energy Chem. **71**, 63–82 (2022). https://doi.org/10.1016/j.jechem.2022.03.041
122. Y. Fang, L. Han, S. Che, Electrocatalytic reduction of CO_2 on chiral Cu surfaces. Chin. J. Struct. Chem. **42**, 100107 (2023). https://doi.org/10.1016/j.cjsc.2023.100107
123. S. Nitopi, E. Bertheussen, S.B. Scott, X. Liu, A.K. Engstfeld et al., Progress and perspectives of electrochemical CO_2 reduction on copper in aqueous electrolyte. Chem. Rev. **119**, 7610–7672 (2019). https://doi.org/10.1021/acs.chemrev.8b00705
124. T.K. Todorova, M.W. Schreiber, M. Fontecave, Mechanistic understanding of CO_2 reduction reaction (CO_2RR) toward multicarbon products by heterogeneous copper-based catalysts. ACS Catal. **10**, 1754–1768 (2020). https://doi.org/10.1021/acscatal.9b04746
125. D. Karapinar, C.E. Creissen, J.G. Rivera de la Cruz, M.W. Schreiber, M. Fontecave, Electrochemical CO_2 reduction to ethanol with copper-based catalysts. ACS Energy Lett. **6**, 694–706 (2021). https://doi.org/10.1021/acsenergylett.0c02610
126. A. Ma, J. Wang, Y. Wang, Y. Zuo, Y. Ren et al., Atomically precise M_{15} (M = Au/Ag/Cu) alloy nanoclusters: structural analysis, optical and electrocatalytic CO_2 reduction properties. Polyoxometalates **3**, 9140054 (2024). https://doi.org/10.26599/pom.2024.9140054
127. Y.-F. Lu, L.-Z. Dong, J. Liu, R.-X. Yang, J.-J. Liu et al., Predesign of catalytically active sites *via* stable coordination cluster model system for electroreduction of CO_2 to ethylene. Angew. Chem. Int. Ed. **60**, 26210–26217 (2021). https://doi.org/10.1002/anie.202111265
128. C.P. Wan, J.D. Yi, R. Cao, Y.B. Huang Conductive metal/covalent organic frameworks for CO_2 electroreduction. Chin. J. Struct. Chem. **41**, 2205001–2205014 (2022). https://doi.org/10.14102/j.cnki.0254-5861.2022-0075
129. K. Yao, J. Li, H. Wang, R. Lu, X. Yang et al., Mechanistic insights into OC-COH coupling in CO_2 electroreduction on fragmented copper. J. Am. Chem. Soc. **144**, 14005–14011 (2022). https://doi.org/10.1021/jacs.2c01044
130. Y.-L. Yang, Y.-R. Wang, L.-Z. Dong, Q. Li, L. Zhang et al., A honeycomb-like porous crystalline hetero-electrocatalyst for efficient electrocatalytic CO_2 reduction. Adv. Mater. **34**, 2206706 (2022). https://doi.org/10.1002/adma.202206706
131. Y.-M. Wang, J. Cai, Q.-Y. Wang, Y. Li, Z. Han et al., Electropolymerization of metal clusters establishing a versatile platform for enhanced catalysis performance. Angew. Chem. Int. Ed. **61**, e202114538 (2022). https://doi.org/10.1002/anie.202114538
132. G. Ma, F. Sun, L. Qiao, Q. Shen, L. Wang et al., Atomically precise alkynyl-protected $Ag_{20}Cu_{12}$ nanocluster: structure analysis and electrocatalytic performance toward nitrate reduction for NH_3 synthesis. Nano Res. **16**, 10867–10872 (2023). https://doi.org/10.1007/s12274-023-5885-6
133. S. Wu, N. Salmon, M.M.-J. Li, R. Bañares-Alcántara, S.C.E. Tsang, Energy decarbonization *via* green H_2 or NH_3? ACS Energy Lett. **7**, 1021–1033 (2022). https://doi.org/10.1021/acsenergylett.1c02816
134. A. Valera-Medina, F. Amer-Hatem, A.K. Azad, I.C. Dedoussi, M. de Joannon et al., Review on ammonia as a potential fuel: from synthesis to economics. Energy Fuels **35**, 6964–7029 (2021). https://doi.org/10.1021/acs.energyfuels.0c03685
135. C. Lv, J. Liu, C. Lee, Q. Zhu, J. Xu et al., Emerging p-block-element-based electrocatalysts for sustainable nitrogen conversion. ACS Nano **16**, 15512–15527 (2022). https://doi.org/10.1021/acsnano.2c07260
136. X. Zhang, Y. Wang, C. Liu, Y. Yu, S. Lu et al., Recent advances in non-noble metal electrocatalysts for nitrate reduction. Chem. Eng. J. **403**, 126269 (2021). https://doi.org/10.1016/j.cej.2020.126269
137. L. Gu, H. Luo, Y. Zhang, Y. Cong, M. Kuang et al., Engineering interfacial architectures toward nitrate electrocatalysis and nitrogen neutral cycle. Mater. Chem. Front. **8**, 1015–1035 (2024). https://doi.org/10.1039/d3qm01038d
138. S. Zhang, Y. Zha, Y. Ye, K. Li, Y. Lin et al., Oxygen-coordinated single Mn sites for efficient electrocatalytic nitrate reduction to ammonia. Nano-Micro Lett. **16**, 9 (2023). https://doi.org/10.1007/s40820-023-01217-z
139. G. Luo, M. Song, Q. Zhang, L. An, T. Shen et al., Advances of synergistic electrocatalysis between single atoms and nanoparticles/clusters. Nano-Micro Lett. **16**, 241 (2024). https://doi.org/10.1007/s40820-024-01463-9
140. T. Wang, H.-J. Wang, J.-S. Lin, J.-L. Yang, F.-L. Zhang et al., Plasmonic photocatalysis: Mechanism, applications and perspectives. Chin. J. Struct. Chem. **42**, 100066 (2023). https://doi.org/10.1016/j.cjsc.2023.100066
141. K. Sun, Y. Qian, H.-L. Jiang, Metal-organic frameworks for photocatalytic water splitting and CO_2 reduction. Angew. Chem. Int. Ed. **62**, e202217565 (2023). https://doi.org/10.1002/anie.202217565
142. J. Chen, L. Lin, P. Lin, L. Xiao, L. Zhang et al., A direct Z-scheme $Bi_2WO_6/La_2Ti_2O_7$ photocatalyst for selective reduction of CO_2 to CO. Chin. J. Struct. Chem. **42**, 100010 (2023). https://doi.org/10.1016/j.cjsc.2022.100010
143. C. Li, J. Wang, L. Tong, Y. Wang, P. Zhang et al., Recent progress and challenges of photocatalytic CO_2 conversion into value-added multi-carbon products. Coord. Chem. Rev. **502**, 215623 (2024). https://doi.org/10.1016/j.ccr.2023.215623
144. M. Sayed, J. Yu, G. Liu, M. Jaroniec, Non-noble plasmonic metal-based photocatalysts. Chem. Rev. **122**, 10484–10537 (2022). https://doi.org/10.1021/acs.chemrev.1c00473

 https://doi.org/10.1007/s40820-024-01555-6

145. L. Zhang, J. Zhang, H. Yu, J. Yu, Emerging S-scheme photocatalyst. Adv. Mater. **34**, e2107668 (2022). https://doi.org/10.1002/adma.202107668
146. C. Ban, Y. Duan, Y. Wang, J. Ma, K. Wang et al., Isotype heterojunction-boosted CO_2 photoreduction to CO. Nano-Micro Lett. **14**, 74 (2022). https://doi.org/10.1007/s40820-022-00821-9
147. M. Gao, F. Tian, X. Zhang, Z. Chen, W. Yang et al., Improved plasmonic hot-electron capture in Au nanoparticle/polymeric carbon nitride by Pt single atoms for broad-spectrum photocatalytic H_2 evolution. Nano-Micro Lett. **15**, 129 (2023). https://doi.org/10.1007/s40820-023-01098-2
148. M. Lu, M. Zhang, J. Liu, T.-Y. Yu, J.-N. Chang et al., Confining and highly dispersing single polyoxometalate clusters in covalent organic frameworks by covalent linkages for CO_2 photoreduction. J. Am. Chem. Soc. **144**, 1861–1871 (2022). https://doi.org/10.1021/jacs.1c11987
149. S. Tao, S. Wan, Q. Huang, C. Li, J. Yu et al., Molecular engineering of g-C_3N_4 with dibenzothiophene groups as electron donor for enhanced photocatalytic H_2-production. Chin. J. Struct. Chem. **41**, 48–54 (2022). https://doi.org/10.14102/j.cnki.0254-5861.2022-0068
150. J.G. Yu, X. Li,, Z.L. Jin,, H.Tang,, E.Z. Liu, Preface to solar photocatalysis. Chin. J. Struct. Chem. **41**, 2206001–2206002 (2022). https://doi.org/10.14102/j.cnki.0254-5861.2022-0158
151. R. Jin, G. Li, S. Sharma, Y. Li, X. Du, Toward active-site tailoring in heterogeneous catalysis by atomically precise metal nanoclusters with crystallographic structures. Chem. Rev. **121**, 567–648 (2021). https://doi.org/10.1021/acs.chemrev.0c00495
152. Y. Du, H. Sheng, D. Astruc, M. Zhu, Atomically precise noble metal nanoclusters as efficient catalysts: a bridge between structure and properties. Chem. Rev. **120**, 526–622 (2020). https://doi.org/10.1021/acs.chemrev.8b00726
153. S. Wang, L. Tang, B. Cai, Z. Yin, Y. Li et al., Ligand modification of Au_{25} nanoclusters for near-infrared photocatalytic oxidative functionalization. J. Am. Chem. Soc. **144**, 3787–3792 (2022). https://doi.org/10.1021/jacs.2c01570
154. Y. Liu, Y. Wang, N. Pinna, Atomically precise metal nanoclusters for photocatalytic water splitting. ACS Mater. Lett. **6**, 2995–3006 (2024). https://doi.org/10.1021/acsmaterialslett.4c00622
155. K.P.S. Cheung, S. Sarkar, V. Gevorgyan, Visible light-induced transition metal catalysis. Chem. Rev. **122**, 1543–1625 (2022). https://doi.org/10.1021/acs.chemrev.1c00403
156. O. Reiser Shining light on copper: unique opportunities for visible-light-catalyzed atom transfer radical addition reactions and related processes. Acc. Chem. Res. **49**, 1990–1996 (2016). https://doi.org/10.1021/acs.accounts.6b00296
157. A. Hossain, A. Bhattacharyya, O. Reiser, Copper's rapid ascent in visible-light photoredox catalysis. Science **364**, eaav9713 (2019). https://doi.org/10.1126/science.aav9713
158. Y. Yun, L. Li, M. Zhou, M. Li, N. Sun et al., Atomically precise coreless AuCu bimetallic nanoclusters for Ullmann C-O coupling. Nano Res. **16**, 10756–10762 (2023). https://doi.org/10.1007/s12274-023-5755-2
159. Z.-J. Guan, J.-J. Li, F. Hu, Q.-M. Wang, Structural engineering toward gold nanocluster catalysis. Angew. Chem. Int. Ed. **61**, e202209725 (2022). https://doi.org/10.1002/anie.202209725
160. S. Zhao, R. Jin, R. Jin, Opportunities and challenges in CO_2 reduction by gold- and silver-based electrocatalysts: from bulk metals to nanoparticles and atomically precise nanoclusters. ACS Energy Lett. **3**, 452–462 (2018). https://doi.org/10.1021/acsenergylett.7b01104
161. Z. Wu, D.-E. Jiang, A.K.P. Mann, D.R. Mullins, Z.-A. Qiao et al., Thiolate ligands as a double-edged sword for CO oxidation on CeO_2 supported $Au_{25}(SCH_2CH_2Ph)_{18}$ nanoclusters. J. Am. Chem. Soc. **136**, 6111–6122 (2014). https://doi.org/10.1021/ja5018706
162. Z. Lei, Q.-M. Wang, Homo and heterometallic gold(I) clusters with hypercoordinated carbon. Coord. Chem. Rev. **378**, 382–394 (2019). https://doi.org/10.1016/j.ccr.2017.11.001
163. A. Ghosh, O.F. Mohammed, O.M. Bakr, Atomic-level doping of metal clusters. Acc. Chem. Res. **51**, 3094–3103 (2018). https://doi.org/10.1021/acs.accounts.8b00412
164. R. Chinchilla, C. Nájera, Recent advances in sonogashira reactions. Chem. Soc. Rev. **40**, 5084–5121 (2011). https://doi.org/10.1039/c1cs15071e
165. B.V. Rokade, J. Barker, P.J. Guiry, Development of and recent advances in asymmetric A3 coupling. Chem. Soc. Rev. **48**, 4766–4790 (2019). https://doi.org/10.1039/c9cs00253g
166. C. Zhang, C. Tang, N. Jiao, Recent advances in copper-catalyzed dehydrogenative functionalization *via* a single electron transfer (SET) process. Chem. Soc. Rev. **41**, 3464–3484 (2012). https://doi.org/10.1039/c2cs15323h
167. R.G. Pearson, Hard and soft acids and bases, HSAB, part 1: fundamental principles. J. Chem. Educ. **45**(9), 581 (1968). https://doi.org/10.1021/ed045p581
168. T. He, Z. Huang, S. Yuan, X.-L. Lv, X.-J. Kong et al., Kinetically controlled reticular assembly of a chemically stable mesoporous Ni(II)-pyrazolate metal–organic framework. J. Am. Chem. Soc. **142**, 13491–13499 (2020). https://doi.org/10.1021/jacs.0c05074
169. P. Hervés, M. Pérez-Lorenzo, L.M. Liz-Marzán, J. Dzubiella, Y. Lu et al., Catalysis by metallic nanoparticles in aqueous solution: model reactions. Chem. Soc. Rev. **41**, 5577–5587 (2012). https://doi.org/10.1039/c2cs35029g
170. X. Kong, J. Liu, Influence of alumina binder content on catalytic performance of Ni/HZSM-5 for hydrodeoxygenation of cyclohexanone. Plos one **9**, e101744 (2014). https://doi.org/10.1371/journal.pone.0101744
171. Y. Kobayashi, S. Tada, M. Kondo, K. Fujiwara, H. Mizoguchi, Intermetallic YIr_2 nanoparticles with negatively charged Ir active sites for catalytic hydrogenation of cyclohexanone to cyclohexanol. Catal. Sci. Technol. **12**, 3088–3093 (2022). https://doi.org/10.1039/d2cy00198e
172. C. Sun, N. Mammen, S. Kaappa, P. Yuan, G. Deng et al., Atomically precise, thiolated copper-hydride nanoclusters as

single-site hydrogenation catalysts for ketones in mild conditions. ACS Nano **13**, 5975–5986 (2019). https://doi.org/10.1021/acsnano.9b02052

173. Y. Li, Z. Tang, P.N. Prasad, M.R. Knecht, M.T. Swihart, Peptide-mediated synthesis of gold nanoparticles: effects of peptide sequence and nature of binding on physicochemical properties. Nanoscale **6**, 3165–3172 (2014). https://doi.org/10.1039/c3nr06201e
174. G. Liao, Y. Gong, L. Zhong, J. Fang, L. Zhang et al., Unlocking the door to highly efficient Ag-based nanoparticles catalysts for $NaBH_4$-assisted nitrophenol reduction. Nano Res. **12**, 2407–2436 (2019). https://doi.org/10.1007/s12274-019-2441-5
175. S.-F. Yuan, Z.-J. Guan, Q.-M. Wang, Identification of the active species in bimetallic cluster catalyzed hydrogenation. J. Am. Chem. Soc. **144**, 11405–11412 (2022). https://doi.org/10.1021/jacs.2c04156
176. X. Chen, Z. Cai, X. Chen, M. Oyama, AuPd bimetallic nanoparticles decorated on graphene nanosheets: their green synthesis, growth mechanism and high catalytic ability in 4-nitrophenol reduction. J. Mater. Chem. A **2**, 5668–5674 (2014). https://doi.org/10.1039/c3ta15141g
177. F. Hu, J.-J. Li, Z.-J. Guan, S.-F. Yuan, Q.-M. Wang, Formation of an alkynyl-protected Ag_{112} silver nanocluster as promoted by chloride released *in situ* from CH_2Cl_2. Angew. Chem. Int. Ed. **59**, 5312–5315 (2020). https://doi.org/10.1002/anie.201915168
178. Q. Zhu, F. Zhang, Y. Huang, H. Xiao, L. Zhao et al., An all-round AI-Chemist with a scientific mind. Natl. Sci. Rev. **9**, nwac190 (2022). https://doi.org/10.1093/nsr/nwac190
179. D. Lockey, C. Mathis, H.N. Miras, L. Cronin, Investigating the autocatalytically driven formation of Keggin-based polyoxometalate clusters. Matter **5**, 302–313 (2022). https://doi.org/10.1016/j.matt.2021.11.030
180. X. Li, S. Takano, T. Tsukuda, Ligand effects on the hydrogen evolution reaction catalyzed by Au_{13} and $Pt@Au_{12}$: alkynyl vs thiolate. J. Phys. Chem. C **125**, 23226–23230 (2021). https://doi.org/10.1021/acs.jpcc.1c08197
181. J.-I. Nishigaki, R. Tsunoyama, H. Tsunoyama, N. Ichikuni, S. Yamazoe et al., A new binding motif of sterically demanding thiolates on a gold cluster. J. Am. Chem. Soc. **134**, 14295–14297 (2012). https://doi.org/10.1021/ja305477a
182. Z. Liu, H. Tan, B. Li, Z. Hu, D.-E. Jiang et al., Ligand effect on switching the rate-determining step of water oxidation in atomically precise metal nanoclusters. Nat. Commun. **14**, 3374 (2023). https://doi.org/10.1038/s41467-023-38914-7
183. S. Yoo, S. Yoo, G. Deng, F. Sun, K. Lee et al., Nanocluster surface microenvironment modulates electrocatalytic CO_2 reduction. Adv. Mater. **36**, e2313032 (2024). https://doi.org/10.1002/adma.202313032
184. W.-Q. Shi, L. Zeng, R.-L. He, X.-S. Han, Z.-J. Guan et al., Near-unity NIR phosphorescent quantum yield from a room-temperature solvated metal nanocluster. Science **383**, 326–330 (2024). https://doi.org/10.1126/science.adk6628
185. S. Hossain, Y. Niihori, L.V. Nair, B. Kumar, W. Kurashige et al., Alloy clusters: precise synthesis and mixing effects. Acc. Chem. Res. **51**, 3114–3124 (2018). https://doi.org/10.1021/acs.accounts.8b00453
186. K. Kwak, W. Choi, Q. Tang, M. Kim, Y. Lee et al., A molecule-like $PtAu_{24}(SC_6H_{13})_{18}$ nanocluster as an electrocatalyst for hydrogen production. Nat. Commun. **8**, 14723 (2017). https://doi.org/10.1038/ncomms14723
187. S. Li, D. Alfonso, A.V. Nagarajan, S.D. House, J.C. Yang et al., Monopalladium substitution in gold nanoclusters enhances CO_2 electroreduction activity and selectivity. ACS Catal. **10**, 12011–12016 (2020). https://doi.org/10.1021/acscatal.0c02266
188. S. Li, A.V. Nagarajan, S. Zhao, G. Mpourmpakis, R. Jin, Understanding the single atom doping effects in oxygen reduction with atomically precise metal nanoclusters. J. Phys. Chem. C **125**, 24831–24836 (2021). https://doi.org/10.1021/acs.jpcc.1c08356
189. Z. Qin, S. Hu, W. Han, Z. Li, W.W. Xu et al., Tailoring optical and photocatalytic properties by single-Ag-atom exchange in $Au_{13}Ag_{12}(PPh_3))_{10}C_{18}$ nanoclusters. Nano Res. **15**, 2971–2976 (2022). https://doi.org/10.1007/s12274-021-3928-4
190. W.L. Zhou, J.J. Jiang, W.R. Cheng, H. Su, Q.H. Liu, In-situ synchrotron radiation infrared spectroscopic identification of reactive intermediates over multiphase electrocatalytic interfaces. Chin. J. Struct. Chem. **41**, 2210004–2210015 (2022). https://doi.org/10.14102/j.cnki.0254-5861.2022-0083
191. L. Xie, C. Huang, Z. Liang, H. Wang, Z. Jiang et al., *In-situ* HP-STM and operando EC-STM studies of heterogeneous catalysis at interfaces. Chin. J. Struct. Chem. **41**, 29–44 (2022). https://doi.org/10.14102/j.cnki.0254-5861.2022-0136
192. Z. Xiao, Y.-C. Huang, C.-L. Dong, C. Xie, Z. Liu et al., *operando* identification of the dynamic behavior of oxygen vacancy-rich Co_3O_4 for oxygen evolution reaction. J. Am. Chem. Soc. **142**, 12087–12095 (2020). https://doi.org/10.1021/jacs.0c00257
193. Y. Yang, S. Louisia, S. Yu, J. Jin, I. Roh et al., operando studies reveal active Cu nanograins for CO_2 electroreduction. Nature **614**, 262–269 (2023). https://doi.org/10.1038/s41586-022-05540-0
194. M. Zhou, T. Higaki, G. Hu, M.Y. Sfeir, Y. Chen et al., Three-orders-of-magnitude variation of carrier lifetimes with crystal phase of gold nanoclusters. Science **364**, 279–282 (2019). https://doi.org/10.1126/science.aaw8007
195. D.-E. Jiang, W. Chen, R.L. Whetten, Z. Chen, What protects the core when the thiolated Au cluster is extremely small? J. Phys. Chem. C **113**, 16983–16987 (2009). https://doi.org/10.1021/jp906823d
196. F. Sun, L. Qin, Z. Tang, G. Deng, M.S. Bootharaju et al., -SR removal or -R removal? A mechanistic revisit on the puzzle of ligand etching of $Au_{25}(SR)_{18}$ nanoclusters during electrocatalysis. Chem. Sci. **14**, 10532–10546 (2023). https://doi.org/10.1039/d3sc03018k

 https://doi.org/10.1007/s40820-024-01555-6